

An Efficient Spatial-Temporal Trajectory Planner for Autonomous Vehicles in Unstructured Environments

Zhichao Han^{*1,2}, Yuwei Wu^{*3}, Tong Li⁴, Lu Zhang⁴, Liua Pei^{1,2},
Long Xu^{1,2}, Chengyang Li², Changjia Ma^{1,2}, Chao Xu^{1,2}, Shaojie Shen⁴, and Fei Gao^{1,2}

Abstract—As a core part of autonomous driving systems, motion planning has received extensive attention from academia and industry. However, real-time trajectory planning capable of spatial-temporal joint optimization is challenged by nonholonomic dynamics, particularly in the presence of unstructured environments and dynamic obstacles. To bridge the gap, we propose a real-time trajectory optimization method that can generate a high-quality whole-body trajectory under arbitrary environmental constraints. By leveraging the differential flatness property of car-like robots, we simplify the trajectory representation and analytically formulate the planning problem while maintaining the feasibility of the nonholonomic dynamics. Moreover, we achieve efficient obstacle avoidance with a safe driving corridor for unmodelled obstacles and signed distance approximations for dynamic moving objects. We present comprehensive benchmarks with State-of-the-Art methods, demonstrating the significance of the proposed method in terms of efficiency and trajectory quality. Real-world experiments verify the practicality of our algorithm. We will release our codes for the research community.¹

Index Terms—Autonomous Vehicles: Motion Planning, Trajectory Optimization, Collision Avoidance.

I. INTRODUCTION

AUTONOMOUS driving has become one of the hottest research topics in recent years because of its vast potential social benefits. It reveals a huge demand for robust and safe motion planning in complex and high-dynamic environments. Moreover, lightweight and efficiency are strongly demanded in real-world applications to ensure rapid response to dynamic and unstructured environments with limited onboard computing power. Motion planning for autonomous driving aims to generate a comfortable, low-energy, and physically feasible trajectory that makes the ego vehicle reach end states with safety guarantees and designed velocities in constrained environments. However, in recent years, only a few approaches are able to generate feasible and high-quality trajectories online in arbitrarily complex scenarios. These existing methods either rely on environmental features with predefined driving rules or oversimplify trajectory generation problems to improve time

^{*} co-first authors.

¹State Key Laboratory of Industrial Control Technology, Zhejiang University, Hangzhou 310027, China. (Corresponding author: Fei Gao)

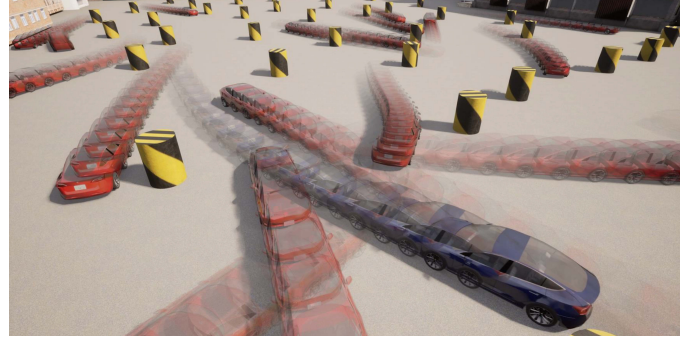
²Huzhou Institute of Zhejiang University, Huzhou 313000, China.

³Department of Electrical and Systems Engineering, University of Pennsylvania, Philadelphia, PA 19104 USA.

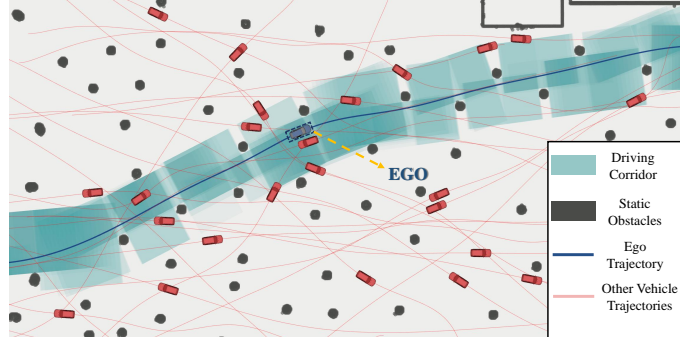
⁴Department of Electronic and Computer Engineering, Hong Kong University of Science and Technology, Hong Kong.

Yuwei Wu contributes to this work during internship at Zhejiang University. E-mail: { zhichaohan, fgaoaa}@zju.edu.cn

¹<https://github.com/ZJU-FAST-Lab/DfTpav>



(a) The movement diagram.



(b) The trajectory visualization.

Fig. 1: The two figures show the capability of our planner in a highly dynamic environment. Because of full-dimensional obstacle avoidance, the ego vehicle has the ability to pass through tight areas near other moving objects while ensuring safety.

efficiency, which cannot be applied to highly constrained unstructured environments. Overall, there is no universal solution for trajectory planning, which makes it the Achilles' heel hindering the development of autonomous driving. In fact, an ideal motion planning for autonomous driving typically faces three challenging problems.

- 1) **Nonholonomic Dynamics:** Unlike holonomic robots such as omnidirectional mobile robots and quadrotors, autonomous vehicles must consider nonholonomic constraints during trajectory planning. Moreover, the strong non-convexity and nonlinearity of nonholonomic dynamics make it difficult to ensure the physical feasibility of states and control inputs in highly constrained environments.
- 2) **Full-Dimensional Obstacle Avoidance:** Safety con-

straints have to balance the accuracy of object shape modeling while maintaining an affordable computation time for online vehicle (re)planning. In real-world applications, rough approximation of the ego vehicle shape, such as one or multiple circular covering of the ego vehicle, always reduces the solution space, which introduces conservativeness or even fails to find a collision-free solution in extremely cluttered areas. While accurate modeling of the ego vehicle and other moving objects increases the complexity of the planning problem, resulting in a significant computation burden.

- 3) **Trajectory Quality:** Time allocation is an inherent attribute of a trajectory. There is always a tradeoff between computation efficiency and trajectory quality. Common methods that optimize time and space separately reduce a large partition of solution space, especially in tightly coupled spatial-temporal scenarios such as highly dynamic environments. By contrast, spatial-temporal joint optimization can fully utilize the solution space to achieve better trajectory optimality but tends to complicate the optimization problem and reduce the real-time performance.

This paper overcomes the above critical issues by proposing an efficient spatial-temporal trajectory planning scheme that generates a trajectory with nonholonomic constraints and achieves obstacle avoidance for full-dimensional objects, as shown in Fig. 1. We parameterize the trajectory on the flat space and encode all feasibility constraints as analytically and continuously differentiable expressions, which are integrated into an optimization formulation. Besides, we model the geometric constraints for static obstacle avoidance and ensure dynamic safety based on the signed distance between the ego vehicle and other dynamic objects. We conduct benchmark comparisons in simulation with other prevalent trajectory planners in different cases to demonstrate the significant superiority of the proposed method. Additionally, we validate our planner on a real platform with fully autonomous onboard computing and no external positioning. The main contributions of this paper can be summarized as follows:

- We present a continuously differentiable spatial-temporal planning formulation in which all constraint can be analytically derived from flat outputs, thus facilitating subsequent efficient optimization.
- We achieve full-shape obstacle avoidance by separating static and dynamic obstacles and using a convex polygon to enclose the ego vehicle. We formulate static safety constraints based on geometric convex decomposition extracted from environments and achieve full-size dynamic avoidance with other moving obstacles by relaxing the sign distance approximation.
- We analyze the characteristics of the constraints in the trajectory planning problem and reformulate the original optimization as an efficiently solvable one without sacrificing optimality.

II. RELATED WORK

A. Trajectory Generations for Vehicles

Sampling-based methods [1]–[11] are widely used for robot motion planning [12] due to the ease of incorporating user-defined objectives. These typical methods, including state lattice approaches and probabilistic planners, always sample the robot state in the configuration space to find a feasible trajectory connecting the starting node and the goal node. Lattice-based planners [1]–[4] discretize the continuous state space into a lattice graph for planning. Then, graph-search algorithms such as Dijkstra are used to obtain the optimal trajectory in the graph. Probabilistic planners [5]–[11] represented by rapidly-exploring random tree (RRT) [5] obtain a feasible path by expanding a state tree rooted at the starting node. Despite the ability to avoid local minima in non-convex space, sampling-based methods confront a dilemma between computation consumption and trajectory quality which limits the direct application in realistic settings.

To simplify the trajectory generation problem, some intuitive approaches [13]–[15] decouple the spatial shape and dynamics profile of the trajectory. Zhu et al. [13] propose convex elastic band smoothing (CES) algorithm which eliminates the non-convexity of the curvature constraint with fixed path lengths at each iteration, and transform the original problem into a quadratically constrained quadratic program (QCQP). However, as presented in work [15], the length consistency assumption does not always hold, which invalidates the curvature constraint and thus reducing the feasibility of the control. Based on CES framework, Zhou et al. [15] propose the dual-loop iterative anchoring path smoothing (DL-IAPS) algorithm to generate a smooth and safe path, where sequential convex optimization (SCP) is used to relax the curvature constraint. Whereas, the efficiency of this method relies heavily on the initial path obtained by hybridA* [17], which limits the application in complex environments.

Highly adaptable model predictive control (MPC) approaches formulate a trajectory planning problem as an optimal control problem (OCP) which is further discretized into a nonlinear programming (NLP) problem. These approaches [18]–[26] directly optimize discrete states and control inputs, which can conveniently integrate dynamic and safety constraints. Although the above MPC-based methods can easily accommodate the motion model of robots, since the trajectory is represented by discrete states, ensuring trajectory constraints in highly constrained environments requires increasing the density of states at the expense of degraded performance.

B. Obstacle Avoidance Formulation

Modeling the ego vehicle and other obstacles determines the complexity of collision-free constraints for trajectory generation problems. Li et al. [26] cover the ego vehicle with two circles along the centerline, and then the ego vehicle model is simplified to two points by inflating obstacles. In the work [26], obstacle avoidance is ensured by constraining these two points within a safe corridor. This approach essentially enjoys the property that the dimension of collision-free constraints is independent of the number of obstacles. However, such a

point-based modeling method does not fully utilize the solution space and often generates overly conservative trajectories, especially in complex environments.

In work [21], they considered the driving scenarios with arbitrarily placed obstacles and formulated the problem as a unified OCP for trajectory generation in unstructured environments. However, the collision-free constraint is nominally non-differentiable. Zhang et al. [28] assume that obstacles are convex and propose an optimization-based collision avoidance (OBCA) algorithm, which removes the integer variables used to model full-dimensional object collision avoidance [29]. They introduce dual variables to reformulate the distance between the robot and obstacles, and transform the safety constraint into a continuous differentiable form. Zhang et al. [24] integrate OBCA into the MPC problem of motion planning and propose H-OBCA, a hierarchical framework for trajectory planning in unstructured environments. Besides, a reasonable method is presented in work [24] for warm-starting dual variables to speed up the optimization. However, the introduction of dual variables in OBCA-based methods [24, 25] increases the dimension of the problem, making it more challenging to solve. Besides, the number of dual variables is positively correlated with the number of obstacles. As obstacles increase, the problem dimension will rise rapidly, leading to unacceptable computational and memory costs.

Instead of sampling the planning state, decouple the spatial and temporal space, discretizing the motion model, or over-relying on the characteristics of environments, our method incorporates spatial-temporal joint optimization to efficiently generate a high-quality trajectory with guaranteed full-dimensional obstacle avoidance. Our method enjoys low computational cost and high robustness against unstructured environments, while more detailed quantitative comparisons are presented in Sect. VII.

III. SPATIAL-TEMPORAL TRAJECTORY PLANNING

In this section, we present the spatial-temporal joint optimization formulation for trajectory planning. To construct the optimization formulation, we discuss the complete motion planning pipeline and introduce the differential flat model of car-like robots. Then, we show the formulation of the trajectory optimization problem in flat-output space considering human comfort, execution time, and feasibility constraints. Last but not least, we analyze the gradient propagation chain of the problem for subsequent numerical optimization.

A. Planning Pipeline

In practical applications, the whole pipeline follows a hierarchical structure with a front-end whose main role is to provide an initial guess, and back-end optimization. We adopt the lightweight hybridA* algorithm to find a collision-free path that is further optimized by the proposed planner. Moreover, for each node to be expanded, we try using Reed Shepp Curve [30] to shoot the end state for the earlier termination of the search process. For complex driving tasks such as autonomous parking, the front-end output often contain both forward and back vehicle movements. By reasonably assuming the vehicle

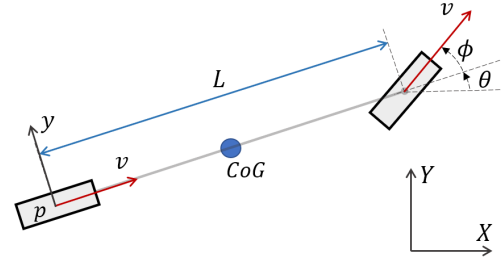


Fig. 2: The kinematic bicycle model.

always reaches a complete stop at the gear shifting position, we parameterize the forward and backward segments of the trajectory as piece-wise polynomials, respectively, whose specific formulations are presented in Sect. III-C. Additionally, the motion direction of each segment is determined by the front-end output and prefixed before the back-end optimization process.

B. Differentially Flat Vehicle Model

We use the simplified kinematic bicycle model in the Cartesian coordinate frame to describe a four-wheel vehicle. Assuming that the car is front-wheel driven and steered with perfect rolling and no slipping, the model can be described as Fig. 2. The state vector is $\mathbf{x} = (p_x, p_y, \theta, v, a_t, a_n, \phi, \kappa)^T$, where $\mathbf{p} = (p_x, p_y)^T$ denotes the position at the center of the rear wheels, v is the longitudinal velocity w.r.t vehicle's body frame, a_t represents the longitude acceleration, a_n is the latitude acceleration, ϕ is the steering angle of the front wheels and κ is the curvature. Thanks to the thorough study of the differentially flat car model [31], we choose the flat output as $\boldsymbol{\sigma} := (\sigma_x, \sigma_y)^T$ with a physical meaning that $\boldsymbol{\sigma} = \mathbf{p}$ is the position centered on the rear wheel of the car. Other variable transformations except p_x, p_y can be expressed as:

$$v = \eta \sqrt{\dot{\sigma}_x^2 + \dot{\sigma}_y^2}, \quad (1a)$$

$$\theta = \arctan 2(\eta \dot{\sigma}_y, \eta \dot{\sigma}_x), \quad (1b)$$

$$a_t = \eta (\dot{\sigma}_x \ddot{\sigma}_x + \dot{\sigma}_y \ddot{\sigma}_y) / \sqrt{\dot{\sigma}_x^2 + \dot{\sigma}_y^2}, \quad (1c)$$

$$a_n = \eta (\dot{\sigma}_x \ddot{\sigma}_y - \dot{\sigma}_y \ddot{\sigma}_x) / \sqrt{\dot{\sigma}_x^2 + \dot{\sigma}_y^2}, \quad (1d)$$

$$\phi = \arctan \left(\eta (\dot{\sigma}_x \ddot{\sigma}_y - \dot{\sigma}_y \ddot{\sigma}_x) L / (\dot{\sigma}_x^2 + \dot{\sigma}_y^2)^{\frac{3}{2}} \right), \quad (1e)$$

$$\kappa = \eta (\dot{\sigma}_x \ddot{\sigma}_y - \dot{\sigma}_y \ddot{\sigma}_x) / (\dot{\sigma}_x^2 + \dot{\sigma}_y^2)^{\frac{3}{2}}. \quad (1f)$$

Consequently, with the natural differential flatness property, we can use the flat outputs and their finite derivatives to characterize arbitrary state quantities of the vehicle, which simplifies the trajectory planning and facilitates optimization. We define an additional variable $\eta \in \{-1, 1\}$ to characterize the motion direction of the vehicle, where $\eta = -1$ and $\eta = 1$ represent the backward and forward movements, respectively. We avoid singularities by fixing the velocity magnitude to a small, non-zero constant when the gear shifts. Both the gear shifting position and directional angle can be optimized, and their specific formulations are presented in Sect. VI-B.

C. Optimization Formulation

The i -th segment of the trajectory is formulated as a 2-dimensional and time-uniform M_i -piece polynomial with degree $N = 2s - 1$, which is parameterized by the intermediate waypoints $\mathbf{q}_i = (\mathbf{q}_{i,1}, \dots, \mathbf{q}_{i,M_i-1}) \in \mathbb{R}^{2 \times (M_i-1)}$, the time interval for each piece $\delta T_i \in \mathbb{R}^+$, and the coefficient matrix $\mathbf{c}_i = (\mathbf{c}_{i,1}^\top, \dots, \mathbf{c}_{i,M_i}^\top)^\top \in \mathbb{R}^{2M_i s \times 2}$. Then, the j -th piece of the i -th segment $\boldsymbol{\sigma}_{i,j}$ is written as:

$$\begin{aligned} \boldsymbol{\sigma}_{i,j}(t) &:= \mathbf{c}_{i,j}^\top \boldsymbol{\beta}(t), \\ \boldsymbol{\beta}(t) &:= (1, t, t^2, \dots, t^N)^\top, \end{aligned} \quad (2)$$

$$\forall t \in [0, \delta T_i], \forall i \in \{1, 2, \dots, n\}, \forall j \in \{1, 2, 3, \dots, M_i\},$$

where n is the number of trajectory segments and $\boldsymbol{\beta}(t)$ is a natural basis. The M_i -piece polynomial trajectory $\boldsymbol{\sigma}_i : [0, T_i]$ is obtained:

$$\begin{aligned} \boldsymbol{\sigma}_i(t) &= \boldsymbol{\sigma}_{i,j}(t - (j-1) * \delta T_i), \\ \forall j \in \{1, 2, \dots, M_i\}, t \in [(j-1) * \delta T_i, j * \delta T_i]. \end{aligned} \quad (3)$$

Here, the total duration of the i -th segment of the trajectory is $T_i = M_i * \delta T_i$. Then, the complete trajectory representation $\boldsymbol{\sigma}(t) : [0, T_s]$ is formulated:

$$\begin{aligned} \boldsymbol{\sigma}(t) &= \boldsymbol{\sigma}_i(t - \hat{T}_i), \\ \forall i \in \{1, 2, \dots, n\}, t \in [\hat{T}_i, \hat{T}_{i+1}), \end{aligned} \quad (4)$$

where $T_s = \sum_{i=1}^n T_i$ is the duration of the whole trajectory, $\hat{T}_i = \sum_{i=1}^{i-1} T_i$ is the timestamp of the starting point of the i -th segment and \hat{T}_1 is set as 0. Moreover, we define a coefficient set $\mathbf{c} = (\mathbf{c}_1^\top, \mathbf{c}_2^\top, \dots, \mathbf{c}_n^\top)^\top \in \mathbb{R}^{(\sum_{i=1}^n 2M_i s) \times 2}$ and a time set $\mathbf{T} = (T_1, T_2, \dots, T_n)^\top \in \mathbb{R}^n$ for the subsequent derivation. With constraints for obstacles avoidance and dynamic feasibility, the minimal control effort problem involving time regularization can be expressed as a nonlinear constrained optimization:

$$\min_{\mathbf{c}, \mathbf{T}} J(\mathbf{c}, \mathbf{T}) = \int_0^{T_s} \boldsymbol{\mu}(t)^\top \mathbf{W} \boldsymbol{\mu}(t) dt + w_T T_s \quad (5a)$$

$$\text{s.t. } \boldsymbol{\mu}(t) = \boldsymbol{\sigma}^{[s]}(t), \forall t \in [0, T_s], \quad (5b)$$

$$\boldsymbol{\sigma}_0^{[s-1]}(0) = \bar{\boldsymbol{\sigma}}_0, \boldsymbol{\sigma}_n^{[s-1]}(T_n) = \bar{\boldsymbol{\sigma}}_f, \quad (5c)$$

$$\boldsymbol{\sigma}_i^{[s-1]}(T_i) = \boldsymbol{\sigma}_{i+1}^{[s-1]}(0) = \tilde{\boldsymbol{\sigma}}_i, 1 \leq i < n, \quad (5d)$$

$$\boldsymbol{\sigma}_{i,j}^{[\bar{d}]}(\delta T_i) = \boldsymbol{\sigma}_{i,j+1}^{[\bar{d}]}(0), 1 \leq i \leq n, 1 \leq j < M_i, \quad (5e)$$

$$T_i > 0, 1 \leq i \leq n, \quad (5f)$$

$$\mathcal{G}_d(\boldsymbol{\sigma}(t), \dots, \boldsymbol{\sigma}^{(s)}(t), t) \leq 0, \quad \forall d \in \mathcal{D}, \forall t \in [0, T_s], \quad (5g)$$

where $\mathbf{W} \in \mathbb{R}^{2 \times 2}$ is a diagonal matrix to penalize control efforts. Eq. (5c) is the boundary condition, where $\bar{\boldsymbol{\sigma}}_0, \bar{\boldsymbol{\sigma}}_f \in \mathbb{R}^{2 \times s}$ are the user-specified initial and final states. $\tilde{\boldsymbol{\sigma}}_i \in \mathbb{R}^{2 \times s}$ is the switching state between forward and reverse gears in which the position and the tangential direction of the motion curve are optimized. Moreover, the specific constraint Eq. (5d) will be described in Sect. VI. Eq. (5e) is the continuity constraint up to degree \bar{d} . The second term $w_T T_s$ in the objective function is the time regularization term to restrict the total duration T_s , with a weight $w_T \in \mathbb{R}^+$. The constraint

function at d is defined as \mathcal{G}_d . In our formulation, the set $\mathcal{D} = \{d : d = v, a_t, a_n, \kappa, \zeta, \Theta\}$ includes dynamic feasibility (v, a_t, a_n, κ), static and dynamic obstacle avoidance (ζ, Θ). Besides, s is chosen as 3, which means that the integration of jerk is minimized to ensure human comfort [32].

D. Gradient Derivation

Without loss of completeness, we first derive the analytic gradients of the objective function J w.r.t $\mathbf{c}_{i,j}$ and T_i :

$$\frac{\partial J}{\partial \mathbf{c}_{i,j}} = 2 \left(\int_0^{\delta T_i} \boldsymbol{\beta}^{(s)}(t) \boldsymbol{\beta}^{(s)}(t)^\top dt \right) \mathbf{c}_{i,j}, \quad (6)$$

$$\frac{\partial J}{\partial T_i} = \frac{1}{M_i} \sum_{j=1}^{M_i} \mathbf{c}_{i,j}^\top \boldsymbol{\beta}^{(s)}(\delta T_i) \boldsymbol{\beta}^{(s)}(\delta T_i)^\top \mathbf{c}_{i,j} + w_T. \quad (7)$$

The feasibility constraints Eq.(5g) imposed on the entire trajectory are equivalent to each piece of any piece-wise polynomial trajectory segment complying with these constraints:

$$\begin{aligned} \mathcal{G}_d(\boldsymbol{\sigma}(t), \dots, \boldsymbol{\sigma}^{(s)}(t), t) \leq 0, \forall d \in \mathcal{D}, \forall t \in [0, T_s] &\iff \\ \mathcal{G}_d(\boldsymbol{\sigma}_{i,j}(\bar{t}), \dots, \boldsymbol{\sigma}_{i,j}^{(s)}(\bar{t}), \hat{t}) \leq 0, \forall d \in \mathcal{D}, \forall \bar{t} \in [0, \delta T_i], \\ \forall i \in \{1, 2, \dots, n\}, \forall j \in \{1, 2, 3, \dots, M_i\}, \end{aligned} \quad (8)$$

where \bar{t} is the relative timestamp and $\hat{t} = \hat{T}_i + \delta T_i * (j-1) + \bar{t}$ is the absolute timestamp. Therefore, to approximate the continuous-time formula Eq. (8), we uniformly discretize each piece of the piece-wise polynomial into $\lambda \in \mathbb{N}_{>0}$ constraint points. Moreover, we ensure trajectory feasibility by imposing constraints on these constraint points. Then, the continuous-time formula Eq. (8) is transformed into a discrete form:

$$\begin{aligned} \mathcal{G}_{d,i,j,k}(\mathbf{c}_{i,j}, \mathbf{T}) &\leq 0, \\ \mathcal{G}_{d,i,j,k}(\mathbf{c}_{i,j}, \mathbf{T}) &:= \mathcal{G}_d(\boldsymbol{\sigma}_{i,j,k}, \dots, \boldsymbol{\sigma}_{i,j,k}^{(s)}, \hat{t}), \\ \boldsymbol{\sigma}_{i,j,k}^{(\bar{d})} &:= \boldsymbol{\sigma}_{i,j}^{(\bar{d})}(\bar{t}), \quad \forall \bar{d} \in \{0, 1, \dots, s\}, \\ \bar{t} &= \frac{k T_i}{\lambda M_i}, \quad \hat{t} = \hat{T}_i + \left(\frac{j-1}{M_i} + \frac{k}{\lambda M_i} \right) T_i, \\ \forall k \in \{0, 1, 2, \dots, \lambda\}, \quad \forall d \in \mathcal{D}. \end{aligned} \quad (9)$$

Without loss of generality, we derive the gradient propagation at any constraint point based on the chain rule:

$$\frac{\partial \mathcal{G}_{d,i,j,k}}{\partial \mathbf{c}_{i,j}} = \sum_{\bar{d}=0}^s \beta^{(\bar{d})}(\bar{t}) \left(\frac{\partial \mathcal{G}_{d,i,j,k}}{\partial \boldsymbol{\sigma}_{i,j,k}^{(\bar{d})}} \right)^\top, \quad (10)$$

$$\frac{\partial \mathcal{G}_{d,i,j,k}}{\partial \mathbf{T}} = \frac{\partial \mathcal{G}_{d,i,j,k}}{\partial \bar{t}} \frac{\partial \bar{t}}{\partial \mathbf{T}} + \frac{\partial \mathcal{G}_{d,i,j,k}}{\partial \hat{t}} \frac{\partial \hat{t}}{\partial \mathbf{T}}, \quad (11)$$

We further derive time-related gradient terms inside Eq. (11):

$$\frac{\partial \mathcal{G}_{d,i,j,k}}{\partial \bar{t}} = \sum_{\bar{d}=0}^s \left(\boldsymbol{\sigma}_{i,j,k}^{(\bar{d}+1)} \right)^\top \frac{\partial \mathcal{G}_{d,i,j,k}}{\partial \boldsymbol{\sigma}_{i,j,k}^{(\bar{d})}}, \quad (12)$$

$$\frac{\partial \bar{t}}{\partial \mathbf{T}} = \left(\mathbf{0}_{i-1}^\top, \frac{k}{\lambda M_i}, \mathbf{0}_{n-i}^\top \right)^\top, \quad (13)$$

$$\frac{\partial \hat{t}}{\partial \mathbf{T}} = \left(\mathbf{1}_{i-1}^\top, \frac{k}{\lambda M_i} + \frac{j-1}{M_i}, \mathbf{0}_{n-i}^\top \right)^\top, \quad (14)$$

where all the above gradient calculations w.r.t vectors follow the denominator layout. As a result, by substituting Eq.(12)-(14) to Eq.(11), we can obtain the gradients of $G_{d,i,j,k}$ w.r.t $\mathbf{c}_{i,j}$ and \mathbf{T} once $\partial G_{d,i,j,k}/\partial \sigma_{i,j,k}^{(\bar{d})}$ and $\partial G_{d,i,j,k}/\partial \bar{t}$ are specified. Besides, it is worth mentioning that constraint functions $G_{d,i,j,k}$ can be precisely expressed by some of the quantities in \bar{t} and $\sigma_{i,j,k}^{(\bar{d})}$, where $\bar{d} \in \{0, 1, 2, \dots, s\}$. Therefore, the gradients w.r.t irrelevant variables are 0 without derivation. In subsequent sections, we present the specific formulation of the constraint functions $\mathcal{G}_{d \in \mathcal{D}}$ and derive gradients. For simplification, i, j, k and relative timestamp \bar{t} are omitted in Sect. IV and Sect. V.

IV. INSTANTANEOUS STATE CONSTRAINTS

In this section, we introduce the instantaneous state constraints for trajectory optimization, where these constraint functions are only related to the instantaneous states of the vehicle.

A. Dynamic Feasibility

1) *Longitude Velocity Limit*: For autonomous driving, the longitude velocity always needs to be limited within a reasonable range because of practical factors such as traffic rules, physical vehicle performance, and environmental uncertainty. Then, the constraint function of longitude velocity at a constraint point is defined as follows:

$$\mathcal{G}_v(\dot{\sigma}) = \dot{\sigma}^T \dot{\sigma} - v_m^2. \quad (15)$$

where v_m is the magnitude of maximal longitude velocity. The gradient of $\mathcal{G}_v(\dot{\sigma})$ is written as:

$$\frac{\partial \mathcal{G}_v}{\partial \dot{\sigma}} = 2\dot{\sigma}. \quad (16)$$

Accordingly, we can obtain the gradients of \mathcal{G}_v by combining Eq.(16) and Eq.(10)-(14).

2) *Acceleration Limit*: The acceleration is always required to be limited to prevent skidding due to friction limits between the tire and the ground. From Eq. (1c)(1d), we define the constraint functions of longitude and latitude acceleration at a constraint point:

$$\mathcal{G}_{a_t}(\dot{\sigma}, \ddot{\sigma}) = \frac{(\ddot{\sigma}^T \dot{\sigma})^2}{\dot{\sigma}^T \dot{\sigma}} - a_{tm}^2, \quad (17)$$

$$\mathcal{G}_{a_n}(\dot{\sigma}, \ddot{\sigma}) = \frac{(\ddot{\sigma}^T \mathbf{B} \dot{\sigma})^2}{\dot{\sigma}^T \dot{\sigma}} - a_{nm}^2, \quad (18)$$

where a_{tm} and a_{nm} are the maximal longitude and latitude acceleration and $\mathbf{B} := \begin{bmatrix} 0 & -1 \\ 1 & 0 \end{bmatrix}$ is an auxiliary antisymmetric matrix. The gradients of $\mathcal{G}_{a_t}(\dot{\sigma}, \ddot{\sigma})$ and $\mathcal{G}_{a_n}(\dot{\sigma}, \ddot{\sigma})$ are derived as :

$$\frac{\partial \mathcal{G}_{a_t}}{\partial \dot{\sigma}} = 2 \frac{\ddot{\sigma}^T \dot{\sigma}}{\|\dot{\sigma}\|_2^2} \ddot{\sigma} - 2 \left(\frac{\ddot{\sigma}^T \dot{\sigma}}{\|\dot{\sigma}\|_2^2} \right)^2 \dot{\sigma}, \quad (19)$$

$$\frac{\partial \mathcal{G}_{a_n}}{\partial \dot{\sigma}} = 2 \frac{\ddot{\sigma}^T \mathbf{B} \dot{\sigma}}{\|\dot{\sigma}\|_2^2} \mathbf{B}^T \ddot{\sigma} - 2 \left(\frac{\ddot{\sigma}^T \mathbf{B} \dot{\sigma}}{\|\dot{\sigma}\|_2^2} \right)^2 \dot{\sigma}, \quad (20)$$

$$\frac{\partial \mathcal{G}_{a_t}}{\partial \ddot{\sigma}} = 2 \frac{\ddot{\sigma}^T \dot{\sigma}}{\|\dot{\sigma}\|_2^2} \dot{\sigma}, \quad \frac{\partial \mathcal{G}_{a_n}}{\partial \ddot{\sigma}} = 2 \frac{\ddot{\sigma}^T \mathbf{B} \dot{\sigma}}{\|\dot{\sigma}\|_2^2} \mathbf{B} \dot{\sigma}. \quad (21)$$

3) *Front Steer Angle Limit*: The front steer angle needs to be limited to ensure the nonholonomic dynamic feasibility of the vehicle. Due to the monotonicity of the tangent function, we restrict the front steer angle by limiting the curvature $\kappa = \tan \phi / L$ in $[-\tan \phi_m / L, \tan \phi_m / L] := [-\kappa_m, \kappa_m]$, where ϕ_m is the preset maximum steer angle and κ_m is the corresponding maximum curvature. Then, the nonholonomic dynamic constraint function \mathcal{G}_κ is expressed as:

$$\mathcal{G}_\kappa(\dot{\sigma}, \ddot{\sigma}) = \left(\frac{\ddot{\sigma}^T \mathbf{B} \dot{\sigma}}{\|\dot{\sigma}\|_2^3} \right)^2 - \kappa_m^2. \quad (22)$$

Furthermore, we derive the gradients w.r.t $\dot{\sigma}$ and $\ddot{\sigma}$:

$$\frac{\partial \mathcal{G}_\kappa}{\partial \dot{\sigma}} = 2 \left(\frac{\ddot{\sigma}^T \mathbf{B} \dot{\sigma}}{\|\dot{\sigma}\|_2^3} \right) \left(\frac{\mathbf{B}^T \ddot{\sigma}}{\|\dot{\sigma}\|_2^3} - 3 \frac{\ddot{\sigma}^T \mathbf{B} \dot{\sigma}}{\|\dot{\sigma}\|_2^5} \dot{\sigma} \right), \quad (23)$$

$$\frac{\partial \mathcal{G}_\kappa}{\partial \ddot{\sigma}} = 2 \left(\frac{\ddot{\sigma}^T \mathbf{B} \dot{\sigma}}{\|\dot{\sigma}\|_2^6} \right) \mathbf{B} \dot{\sigma}. \quad (24)$$

B. Static Obstacle Avoidance

In this subsection, we analytically present static safety constraints that are efficiently computable based on the geometric representation of the free space in the environment. We first decompose the semantic environment and extract the safe space to construct a driving corridor consisting of a series of convex polygons. Then, we derive the necessary and sufficient condition for enforcing the full vehicle shape in the driving corridor, which is used to construct static no-collision constraints. Before specific derivation, we introduce the pipeline of the constraint modeling. We first discretize the collision-free path generated by the front end into sampling points whose number is the same as the number of constraint points in the back-end optimization. Then, combined with the environmental information, we generate a free convex polygon based on the sampling point by the method [33] or directly expanding in each defined direction. As a result, the entire trajectory is guaranteed to be safe by confining the full vehicle shape at each constraint point to the corresponding convex polygon, as shown in Fig. 3. We use a convex polygon to enclose the full shape of the ego vehicle which is defined as \mathbb{E} . Moreover, we define the vertex set \mathcal{E} of the convex polygon as:

$$\mathcal{E} = \{v_e \in \mathbb{R}^2 : v_e = \sigma + \mathbf{R}l_e, e = 1, 2, \dots, n_e\}, \quad (25)$$

where \mathbf{R} is the rotation matrix from the body to the world frame, transformed into flat outputs as:

$$\mathbf{R} = \frac{\eta}{\|\dot{\sigma}\|_2} (\dot{\sigma}, \mathbf{B} \dot{\sigma}). \quad (26)$$

Here, n_e is the number of vertexes, and l_e is the coordinate of the e -th vertex in the body frame. $\eta \in \{-1, 1\}$ is a prefixed auxiliary variable to indicate the motion direction of the segment of the trajectory. Note n_e and l_e are also constant once the vehicle shape is identified. The H-representation [34] of each convex polygon \mathcal{P}^H in the driving corridor is obtained:

$$\begin{aligned} \mathcal{P}^H &= \{q \in \mathbb{R}^2 : \mathbf{A}q \leq \mathbf{b}\}, \\ \mathbf{A} &= (\mathbf{A}_1, \dots, \mathbf{A}_z, \dots, \mathbf{A}_{n_z})^T \in \mathbb{R}^{n_z \times 2}, \\ \mathbf{b} &= (b_1, \dots, b_z, \dots, b_{n_z})^T \in \mathbb{R}^{n_z}, \end{aligned} \quad (27)$$

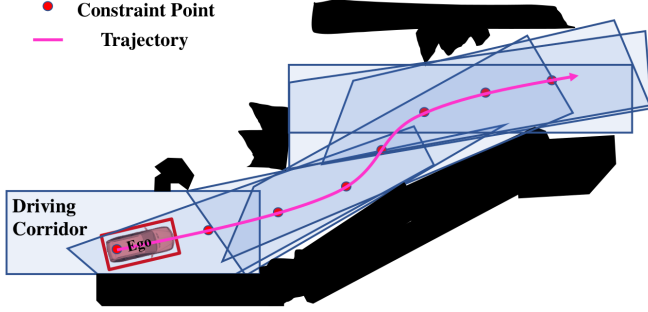


Fig. 3: Visualization of the safe driving corridor. The convex polygon contains the full shape of the ego vehicle at any constraint point. With a proper trajectory resolution, we can practically guarantee the static no-collision property.

where n_z is the number of hyperplanes, $\mathbf{A}_z \in \mathbb{R}^2$ and $b_z \in \mathbb{R}$ are the descriptors of a hyperplane, which can be determined by a point on the hyperplane and the normal vector. Additionally, once the driving corridor is generated, the hyperplane descriptors \mathbf{A}_z and b_z are also completely determined. A sufficient and necessary condition for containing the full shape of the vehicle in a convex polygon is that each vertex of the vehicle shape is contained in the convex polygon:

$$\begin{aligned} \mathbb{E} \subseteq \mathcal{P}^H &\iff \\ \boldsymbol{\sigma} + \mathbf{R}\mathbf{l}_e \subseteq \mathcal{P}^H &\quad \forall e \in \{1, 2, \dots, n_e\}. \end{aligned} \quad (28)$$

A sufficient and necessary condition for containing a vertex in a convex polygon is that the vertex is on the inner side of each hyperplane:

$$\begin{aligned} \boldsymbol{\sigma} + \mathbf{R}\mathbf{l}_e \subseteq \mathcal{P}^H &\iff \\ \mathbf{A}_z^T (\boldsymbol{\sigma} + \mathbf{R}\mathbf{l}_e) \leq b_z &\quad \forall z \in \{1, 2, \dots, n_z\}. \end{aligned} \quad (29)$$

Therefore, the spatial constraint function at a constraint point is $\mathcal{G}_\zeta = (\mathcal{G}_{\zeta_{1,1}}, \dots, \mathcal{G}_{\zeta_{e,z}}, \dots, \mathcal{G}_{\zeta_{n_e, n_z}})^T \in \mathbb{R}^{n_e n_z}$, with $n_e n_z$ linear constraint penalty about vertices of the ego vehicle, which is defined as:

$$\mathcal{G}_{\zeta_{e,z}}(\boldsymbol{\sigma}, \dot{\boldsymbol{\sigma}}) = \mathbf{A}_z^T (\boldsymbol{\sigma} + \mathbf{R}\mathbf{l}_e) - b_z. \quad (30)$$

Before further derivation, we define an auxiliary expression $\mathcal{F}(\mathbf{l}) : \mathbb{R}^2 \rightarrow \mathbb{R}^{2 \times 2}$ to simplify the form:

$$\mathcal{F}(\mathbf{l}) = \frac{\boldsymbol{\eta}(\mathbf{l}, \mathbf{B}\mathbf{l})^T}{\|\dot{\boldsymbol{\sigma}}\|_2} - \frac{\dot{\boldsymbol{\sigma}}(\mathbf{R}\mathbf{l})^T}{\|\dot{\boldsymbol{\sigma}}\|_2^2}. \quad (31)$$

The gradients of the constraint function w.r.t $\boldsymbol{\sigma}$ and $\dot{\boldsymbol{\sigma}}$ are:

$$\frac{\partial \mathcal{G}_{\zeta_{e,z}}}{\partial \boldsymbol{\sigma}} = \mathbf{A}_z, \quad (32)$$

$$\frac{\partial \mathcal{G}_{\zeta_{e,z}}}{\partial \dot{\boldsymbol{\sigma}}} = \mathcal{F}(\mathbf{l}_e) \mathbf{A}_z. \quad (33)$$

The gradients w.r.t the polynomial coefficients and durations can also be calculated by propagating equations Eq.(10)-(14).

V. DYNAMIC OBSTACLE AVOIDANCE

Dynamic safety is guaranteed by ensuring that the minimum distance between the ego vehicle and obstacle convex polygons at each moment of the trajectory is greater than the safety threshold. To increase readability, we introduce helpful priors for evaluating the signed distance between convex polygons. Then, we elaborate on the dynamic avoidance constraint function which is further relaxed into a continuously differentiable form.

A. Preliminaries on Distance Representations

1) *Signed Distances for Rigid Objects*: We consider two convex polytopes \mathbb{E}, \mathbb{O} bounded by the intersection of half-spaces, as $\mathbb{E} = \bigcap_{e=1}^{K_e} \mathcal{P}_e$, $\mathbb{O} = \bigcap_{o=1}^{K_o} \mathcal{P}_o$. The usual convex collision avoidance method penalizes the signed distance between two sets. The distance is defined with the minimal translation \mathcal{T} as:

$$\text{dist}(\mathbb{E}, \mathbb{O}) = \min_{\mathcal{T}} \{\|\mathcal{T}\| : (\mathbb{E} + \mathcal{T}) \cap \mathbb{O} \neq \emptyset\}. \quad (34)$$

When overlapping, $\text{dist} = 0$ holds, which is insufficient to obtain gradient directions to separate them. The penetration depth can be combined to solve this issue:

$$\text{pen}(\mathbb{E}, \mathbb{O}) = \min_{\mathcal{T}} \{\|\mathcal{T}\| : (\mathbb{E} + \mathcal{T}) \cap \mathbb{O} = \emptyset\}. \quad (35)$$

Hence, we can get the signed distance:

$$\text{sd}(\mathbb{E}, \mathbb{O}) := \text{dist}(\mathbb{E}, \mathbb{O}) - \text{pen}(\mathbb{E}, \mathbb{O}). \quad (36)$$

Computing the signed distance requires solving minimum optimization problems Eq. (34, 35), which is unsuitable for embedding into our trajectory optimization problem. We will discuss a Minkowski difference-based algorithm for the approximate efficient computation of signed distances in the next section.

2) *Approximation Distances*: We follow the definition of Minkowski difference used in GJK algorithm [35]. Considering the general case where $A, B \in \mathbb{R}^n$ are two sets, the Minkowski Difference is defined by:

$$A - B = \{a - b \in \mathbb{R}^n : a \in A, b \in B\}. \quad (37)$$

Based on the core property [36] extensively used for collision checking:

$$\text{sd}(\mathbb{E}, \mathbb{O}) = \text{sd}(\mathbf{0}, \mathbb{O} - \mathbb{E}). \quad (38)$$

The problem of computing signed distances between two sets can be reduced to the distance between the origin point $\mathbf{0}$ to the set $\mathbb{O} - \mathbb{E}$. A concise formulation to bound signed distances is proposed in [37], defined as the maximum signed distance from the origin to the Minkowski difference between a polygon and each hyperplane:

$$\begin{aligned} \max_{\mathcal{P}_e, \mathcal{P}_o} \{\text{sd}(\mathbf{0}, \mathbb{O} - \mathcal{P}_e), \text{sd}(\mathbf{0}, \mathcal{P}_o - \mathbb{E})\} &\leq \text{sd}(\mathbb{E}, \mathbb{O}), \\ \forall e &= \{1, \dots, K_e\}, \forall o = \{1, \dots, K_o\}. \end{aligned} \quad (39)$$

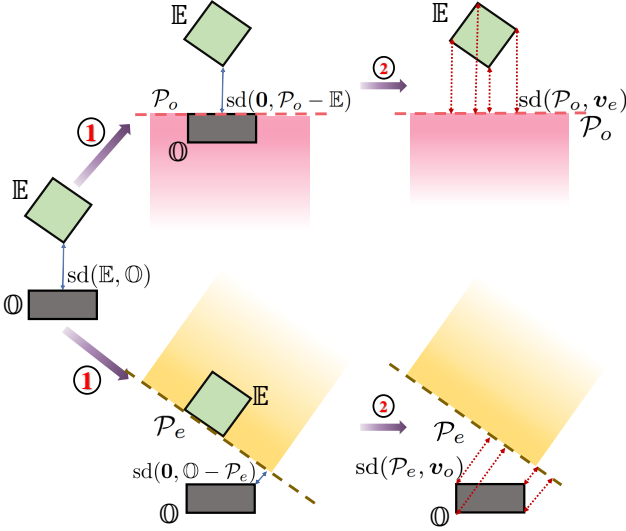


Fig. 4: Illustration of computing the lower bound of the signed distance between convex sets \mathbb{E} and \mathbb{O} , where \mathcal{P}_e and \mathcal{P}_o refer to any hyperplane of \mathbb{E} and \mathbb{O} . Besides, we define \mathbf{v}_e and \mathbf{v}_o as any vertex of \mathbb{E} and \mathbb{O} , respectively. The computation process follows the above two-stage structure. We first use the maximum of the signed distances between convex sets and hyperplanes to approximate $\text{sd}(\mathbb{E}, \mathbb{O})$. Then, due to the convexity of \mathbb{E} and \mathbb{O} , $\text{sd}(\mathbb{O}, \mathcal{P}_o - \mathbb{E})$ and $\text{sd}(\mathbb{O}, \mathbb{O} - \mathcal{P}_e)$ are converted to point-to-hyperplane distances $\text{sd}(\mathcal{P}_o, \mathbf{v}_e)$ and $\text{sd}(\mathcal{P}_e, \mathbf{v}_o)$ which can be analytically calculated.

By extending the Minkowski difference to the case between a polygon and each hyperplane, we have

$$\begin{aligned} \mathbb{O} - \mathcal{P}_e &= \{\mathbf{p} \in \mathbb{R}^n : \mathbf{p} + \mathbf{y} \in \mathbb{O}, \mathbf{y} \in \mathcal{P}_e\}, \\ &= \{\mathbf{p} \in \mathbb{R}^n : (\mathbf{H}^e)^T \mathbf{p} \geq -h^e + (\mathbf{H}^e)^T \mathbf{u}, \mathbf{u} \in \mathbb{O}\}. \end{aligned} \quad (40)$$

with $\mathcal{P}_e = \{\mathbf{y} \in \mathbb{R}^n : (\mathbf{H}^e)^T \mathbf{y} \leq h^e\}$ as a hyperplane of the set \mathbb{E} . Similarly, we obtain

$$\mathcal{P}_o - \mathbb{E} = \{\mathbf{p} \in \mathbb{R}^n : (\mathbf{G}^o)^T \mathbf{p} \leq g^o - (\mathbf{G}^o)^T \mathbf{y}, \mathbf{y} \in \mathbb{E}\}. \quad (41)$$

The signed distance can be computed as:

$$\text{sd}(\mathbb{O}, \mathbb{O} - \mathcal{P}_e) = \frac{1}{\|\mathbf{H}^e\|_2} (-h^e + \min_{\mathbf{u}} (\mathbf{H}^e)^T \mathbf{u}), \quad (42)$$

$$\text{sd}(\mathbb{O}, \mathcal{P}_o - \mathbb{E}) = \frac{1}{\|\mathbf{G}^o\|_2} (-g^o + \min_{\mathbf{y}} (\mathbf{G}^o)^T \mathbf{y}). \quad (43)$$

The physical meaning of this formulation is that the signed distance of two sets is bounded by a maximum signed distance of one set to each hyperplane and vice versa. For convex polytopes, we only need to check each vertex to get the minimum value and then the lower bound can be analytically calculated for optimization, as shown in Fig. 4.

B. Constraint for Dynamic Avoidance

We apply discrete obstacle avoidance constraints on the constraint points along the trajectory regarding the trajectories of other obstacles at the same time stamp. Therefore,

the dynamic safety constraint is defined as $\mathcal{G}_{\Theta}(\boldsymbol{\sigma}, \dot{\boldsymbol{\sigma}}, \hat{t}) = \{\mathcal{G}_{\Theta_1}, \dots, \mathcal{G}_{\Theta_u}, \dots, \mathcal{G}_{\Theta_{N_u}}\}^T \in \mathbb{R}^{N_u}$ where N_u is the number of dynamic obstacles. The dynamic avoidance constraint function with the u -th moving object at a constraint point is defined as:

$$\mathcal{G}_{\Theta_u}(\boldsymbol{\sigma}, \dot{\boldsymbol{\sigma}}, \hat{t}) = d_m - U(\mathbb{E}(\boldsymbol{\sigma}, \dot{\boldsymbol{\sigma}}), \mathbb{O}_u(\hat{t})), \quad (44)$$

where d_m is the minimum safe distance (safety margin) and $U(\mathbb{E}(t), \mathbb{O}_u(t))$ is the distance between the ego vehicle and the moving obstacle. With the lower approximation of the signed distance between two convex objects (Sect. V-A2), we have:

$$\text{sd}(\mathbb{E}(\boldsymbol{\sigma}, \dot{\boldsymbol{\sigma}}), \mathbb{O}_u(\hat{t})) \geq \text{lb}_{\text{sd}}(\mathbb{E}(\boldsymbol{\sigma}, \dot{\boldsymbol{\sigma}}), \mathbb{O}_u(\hat{t})). \quad (45)$$

The lower bound lb_{sd} is paraphrased by Eq. (39) as:

$$\begin{aligned} \text{lb}_{\text{sd}}(\mathbb{E}(\boldsymbol{\sigma}, \dot{\boldsymbol{\sigma}}), \mathbb{O}_u(\hat{t})) &= \\ & \max_{\mathcal{P}_e, \mathcal{P}_o^u} \{\text{sd}(\mathbb{O}_u(\hat{t}) - \mathcal{P}_e(\boldsymbol{\sigma}, \dot{\boldsymbol{\sigma}}), \text{sd}(\mathbb{O}, \mathcal{P}_o^u(\hat{t}) - \mathbb{E}(\boldsymbol{\sigma}, \dot{\boldsymbol{\sigma}}))\}, \\ & e \in \{1, \dots, n_e\}, o \in \{1, \dots, n_u\}, \end{aligned} \quad (46)$$

where n_u is the number of hyperplanes of the u -th moving obstacle and \mathcal{P}_o^u is the hyperplane. Since the motion planning is on a two-dimensional plane, a hyperplane of a convex set degenerates into a straight line determined by two vertices. Then, the hyperplane descriptors of the ego vehicle can be determined as follows:

$$\mathbf{H}^e = \frac{\mathbf{B}(\mathbf{v}_{e+1} - \mathbf{v}_e)}{\|\mathbf{v}_{e+1} - \mathbf{v}_e\|_2}, \quad (47)$$

$$\mathbf{h}^e = (\mathbf{H}^e)^T \mathbf{v}_e, e \in \{1, \dots, n_e\}, \quad (48)$$

where $\{\mathbf{v}_1, \dots, \mathbf{v}_e, \dots, \mathbf{v}_{n_e+1}\}$ are the vertices arranged clockwise, defined in Sec.IV-B, and $\mathbf{v}_{n_e+1} = \mathbf{v}_1$. Due to the convexity of the model, the distance between the moving obstacle and the hyperplane is converted into the minimum distance between vertices and the hyperplane, thus simplifying Eq.(42):

$$\begin{aligned} \text{sd}(\mathbb{O}_u - \mathcal{P}_e) &= \frac{1}{\|\mathbf{H}^e\|_2} (-h^e + \min_o (\mathbf{H}^e)^T \mathbf{v}_o^u), \\ \mathbf{v}_o^u &= \mathbf{w}_u + \mathbf{R}_u \mathbf{l}_o^u, \quad o \in \{1, \dots, n_u\}, \end{aligned} \quad (49)$$

where \mathbf{v}_o^u is any vertex of the moving obstacle \mathbb{O}_u . \mathbf{w}_u and \mathbf{R}_u are the origin and rotation matrix of the obstacle body coordinate system, respectively. \mathbf{l}_o^u is the translation vector determined in advance. Before further derivation, we define an auxiliary expression $\mathcal{H}(\tilde{\mathbf{R}}, \Delta \mathbf{l}) : (\mathbb{R}^{2 \times 2}, \mathbb{R}^2) \rightarrow \mathbb{R}^2$:

$$\mathcal{H}(\tilde{\mathbf{R}}, \Delta \mathbf{l}) = \frac{\mathbf{B} \tilde{\mathbf{R}} \Delta \mathbf{l}}{\|\Delta \mathbf{l}\|_2}. \quad (50)$$

By combining Eq.(25)(47-49), the signed distance can be analytically calculated:

$$\text{sd}(\mathbb{O}_u - \mathcal{P}_e) = \min_o \mathcal{H}(\mathbf{R}_u, \Delta \mathbf{l}_e)^T (\mathbf{v}_o^u - \mathbf{v}_e), \quad (51)$$

where $\Delta \mathbf{l}_e = \mathbf{l}_{e+1} - \mathbf{l}_e$, and the physical meaning of $\mathcal{H}(\mathbf{R}_u, \Delta \mathbf{l}_e)$ is the normal vector outwards of the plane \mathcal{P}_e . Similarly, the signed distance between \mathcal{P}_o^u and \mathbb{E} can also be obtained:

$$\text{sd}(\mathbb{O}_u - \mathcal{P}_e) = \min_e \mathcal{H}(\mathbf{R}_u, \Delta \mathbf{l}_e^u)^T (\mathbf{v}_e - \mathbf{v}_o^u). \quad (52)$$

Finally, we substitute Eq.(51)(52) into Eq.(46) to obtain the analytical expression of lb_{sd} :

$$\begin{aligned} \text{lb}_{\text{sd}}(\mathbb{E}(\boldsymbol{\sigma}, \dot{\boldsymbol{\sigma}}), \mathbb{O}_u(\hat{t})) = & \\ \max\{\max_e \min_o \mathcal{H}(\mathbf{R}, \Delta \mathbf{l}_e)^T (\mathbf{v}_o^u(\hat{t}) - \mathbf{v}_e), & \\ \max_o \min_e \mathcal{H}(\mathbf{R}_u(\hat{t}), \Delta \mathbf{l}_o^u)^T (\mathbf{v}_e - \mathbf{v}_o^u(\hat{t}))\}, & \\ e \in \{1, \dots, n_e\}, o \in \{1, \dots, n_u\}. & \end{aligned} \quad (53)$$

To smooth the maximum and minimum operations, a widely adopted log-sum-exp function is applied, defined as follows to approximate the vector-max(min) function:

$$\text{lse}_\alpha(\boldsymbol{\gamma}) = \alpha^{-1} \log \left(\sum_{\omega=1}^{\Omega} \exp(\alpha r_\omega) \right), \quad (54)$$

where r_ω is a element of the vector $\boldsymbol{\gamma} = \{r_1, \dots, r_\omega, \dots, r_\Omega\}^T \in \mathbb{R}^{\Omega > 0}$. if $\alpha > 0$ then it approximately gets the maximum value in $\boldsymbol{\gamma}$, or $\alpha < 0$ selects the minimum term. We smooth the discrete function by the log-sum-exp function with the advantage that the gradient of the log-sum-exp function is exactly the softmax(min) function. Moreover, the approximation error of the log-sum-exp is lower bounded by:

$$\text{lse}_{\alpha > 0}(\boldsymbol{\gamma}) \geq \max\{\boldsymbol{\gamma}\} \geq \text{lse}_{\alpha > 0}(\boldsymbol{\gamma}) - \frac{\log(\Omega)}{\alpha}. \quad (55)$$

Hence, we can formulate the distance function:

$$\begin{aligned} U(\mathbb{E}(\boldsymbol{\sigma}, \dot{\boldsymbol{\sigma}}), \mathbb{O}_u(\hat{t})) = \text{lse}_{\alpha > 0}(\mathbf{d}) - \frac{\log(n_e + n_u)}{\alpha}, \\ \mathbf{d} = (\mathbf{d}_U^T, \mathbf{d}_E^T)^T \in \mathbb{R}^{n_e + n_u}, \\ \mathbf{d}_U = (d_U^1, \dots, d_U^e, \dots, d_U^{n_e})^T \in \mathbb{R}^{n_e}, \\ \mathbf{d}_E = (d_E^1, \dots, d_E^e, \dots, d_E^{n_u})^T \in \mathbb{R}^{n_u}, \end{aligned} \quad (56)$$

where $d_U^e = \text{sd}(\mathbf{0}, \mathbb{O}_u(\hat{t}) - \mathcal{P}_e(\boldsymbol{\sigma}, \dot{\boldsymbol{\sigma}}))$ and $d_E^e = \text{sd}(\mathbf{0}, \mathcal{P}_o^u(\hat{t}) - \mathbb{E}(\boldsymbol{\sigma}, \dot{\boldsymbol{\sigma}}))$ are defined to simplify the formulation. Similarly, the minimum operation in d_U^e and d_E^e can be approximated by the log-sum-exp function with $\alpha < 0$. Combined with Eq.(51)(52) We transform the distance into the flat-output space as:

$$\begin{aligned} d_U^e &= \text{lse}_{\alpha < 0} \left((d_{U_1}^e, \dots, d_{U_o}^e, \dots, d_{U_{n_u}}^e)^T \right) + \tilde{d}_U^e, \\ d_E^e &= \text{lse}_{\alpha < 0} \left((d_{E_1}^e, \dots, d_{E_e}^e, \dots, d_{E_{n_e}}^e)^T \right) + \tilde{d}_E^e, \\ d_{U_o}^e &= \mathcal{H}(\mathbf{R}, \Delta \mathbf{l}_e)^T \mathbf{R}_u(\hat{t}) \mathbf{l}_o^u, \\ d_{E_e}^e &= \mathcal{H}(\mathbf{R}_u(\hat{t}), \Delta \mathbf{l}_o^u)^T \mathbf{R} \mathbf{l}_e, \\ \tilde{d}_U^e &= \mathcal{H}(\mathbf{R}, \Delta \mathbf{l}_e)^T (\mathbf{w}_u(\hat{t}) - \mathbf{v}_e), \\ \tilde{d}_E^e &= \mathcal{H}(\mathbf{R}_u(\hat{t}), \Delta \mathbf{l}_o^u)^T (\boldsymbol{\sigma} - \mathbf{v}_o^u(\hat{t})). \end{aligned} \quad (57)$$

By substituting Eq.(57) into Eq.(56) and then into Eq.(44), $\mathcal{G}_{\Theta_u}(\boldsymbol{\sigma}, \dot{\boldsymbol{\sigma}}, \hat{t})$ is transformed into a continuously differentiable function that can be analytically expressed by flat outputs. Based on the chain rule, we calculate the gradients:

$$\begin{aligned} \frac{\partial \mathcal{G}_{\Theta_u}}{\partial \boldsymbol{\sigma}} &= - \sum_{e=1}^{n_e} \text{lse}'_{\alpha > 0}(d_U^e) \frac{\partial \tilde{d}_U^e}{\partial \boldsymbol{\sigma}} - \sum_{o=1}^{n_u} \text{lse}'_{\alpha > 0}(d_E^o) \frac{\partial \tilde{d}_E^o}{\partial \boldsymbol{\sigma}}, \\ \frac{\partial \tilde{d}_U^e}{\partial \boldsymbol{\sigma}} &= -\mathcal{H}(\mathbf{R}, \Delta \mathbf{l}_e), \quad \frac{\partial \tilde{d}_E^o}{\partial \boldsymbol{\sigma}} = \mathcal{H}(\mathbf{R}_u(\hat{t}), \Delta \mathbf{l}_o^u), \end{aligned} \quad (58)$$

where $\text{lse}' : \mathbb{R} \rightarrow \mathbb{R}$ is the gradient of the log-sum-exp function. In a similar way, we derive the gradients w.r.t \hat{t} and

$\dot{\boldsymbol{\sigma}}$:

$$\begin{aligned} \frac{\partial \mathcal{G}_{\Theta_u}}{\partial \hat{t}} &= - \sum_{e=1}^{n_e} \text{lse}'_{\alpha > 0}(d_U^e) \left(\sum_{o=1}^{n_u} \text{lse}'_{\alpha < 0}(d_{U_o}^e) \frac{\partial d_{U_o}^e}{\partial \hat{t}} + \frac{\partial \tilde{d}_U^e}{\partial \hat{t}} \right) \\ &\quad - \sum_{o=1}^{n_u} \text{lse}'_{\alpha > 0}(d_E^o) \left(\sum_{e=1}^{n_e} \text{lse}'_{\alpha < 0}(d_{E_e}^o) \frac{\partial d_{E_e}^o}{\partial \hat{t}} + \frac{\partial \tilde{d}_E^o}{\partial \hat{t}} \right), \\ \frac{\partial \mathcal{G}_{\Theta_u}}{\partial \dot{\boldsymbol{\sigma}}} &= - \sum_{e=1}^{n_e} \text{lse}'_{\alpha > 0}(d_U^e) \left(\sum_{o=1}^{n_u} \text{lse}'_{\alpha < 0}(d_{U_o}^e) \frac{\partial d_{U_o}^e}{\partial \dot{\boldsymbol{\sigma}}} + \frac{\partial \tilde{d}_U^e}{\partial \dot{\boldsymbol{\sigma}}} \right) \\ &\quad - \sum_{o=1}^{n_u} \text{lse}'_{\alpha > 0}(d_E^o) \sum_{e=1}^{n_e} \text{lse}'_{\alpha < 0}(d_{E_e}^o) \frac{\partial d_{E_e}^o}{\partial \dot{\boldsymbol{\sigma}}}. \end{aligned} \quad (59)$$

From Eq.(59), we can obtain the gradients of the dynamic safety constraint once the gradients of auxiliary distances are determined. Next, we derive the gradients w.r.t $\dot{\boldsymbol{\sigma}}$:

$$\begin{aligned} \frac{\partial d_{U_o}^e}{\partial \dot{\boldsymbol{\sigma}}} &= \frac{\mathcal{F}(\Delta \mathbf{l}_e) \mathbf{B}^T \mathbf{R}_u(\hat{t}) \mathbf{l}_o^u}{\|\Delta \mathbf{l}_e\|_2}, \\ \frac{\partial \tilde{d}_U^e}{\partial \dot{\boldsymbol{\sigma}}} &= \frac{\mathcal{F}(\Delta \mathbf{l}_e) \mathbf{B}^T (\mathbf{w}_u(\hat{t}) - \mathbf{v}_e) + \mathcal{F}(\mathbf{l}_e) \mathbf{B}^T \mathbf{R} \Delta \mathbf{l}_e}{\|\Delta \mathbf{l}_e\|_2}, \\ \frac{\partial d_{E_e}^o}{\partial \dot{\boldsymbol{\sigma}}} &= \mathcal{F}(\mathbf{l}_e) \mathcal{H}(\mathbf{R}_u(\hat{t}), \Delta \mathbf{l}_o^u). \end{aligned} \quad (60)$$

Then, the gradients w.r.t abstract timestamp \hat{t} are also derived as follows:

$$\begin{aligned} \frac{\partial d_{U_o}^e}{\partial \hat{t}} &= \left(\dot{\mathbf{R}}_u(\hat{t}) \mathbf{l}_o^u \right)^T \mathcal{H}(\mathbf{R}, \Delta \mathbf{l}_e), \\ \frac{\partial \tilde{d}_U^e}{\partial \hat{t}} &= \left(\dot{\mathbf{w}}_u(\hat{t}) \right)^T \mathcal{H}(\mathbf{R}, \Delta \mathbf{l}_e), \\ \frac{\partial d_{E_e}^o}{\partial \hat{t}} &= \left(\mathbf{R} \mathbf{l}_e \right)^T \mathcal{H}(\dot{\mathbf{R}}_u(\hat{t}), \Delta \mathbf{l}_o^u), \\ \frac{\partial \tilde{d}_E^o}{\partial \hat{t}} &= \mathcal{H}(\dot{\mathbf{R}}_u(\hat{t}), \Delta \mathbf{l}_o^u)^T (\boldsymbol{\sigma} - \mathbf{w}_u(\hat{t}) - \mathbf{R}_u(\hat{t}) \mathbf{l}_o^u) \\ &\quad - \mathcal{H}(\mathbf{R}_u(\hat{t}), \Delta \mathbf{l}_o^u)^T (\dot{\mathbf{w}}_u(\hat{t}) + \dot{\mathbf{R}}_u(\hat{t}) \mathbf{l}_o^u), \end{aligned} \quad (61)$$

where $\dot{\mathbf{R}}_u(\hat{t}) \in \mathbb{R}^{2 \times 2}$ and $\dot{\mathbf{w}}_u(\hat{t}) \in \mathbb{R}^2$ are the gradients w.r.t \hat{t} . In practice, trajectories of other obstacles are fitted by piecewise polynomials. Therefore, the position $\mathbf{w}_u(\hat{t})$, the rotation matrix $\mathbf{R}_u(\hat{t})$ and their gradients can also be calculated analytically. Besides, we set α as 100 to approximate the maximum function and -100 to smooth the minimum function.

VI. REFORMULATION OF TRAJECTORY OPTIMIZATION

In this section, we analyze the characteristics of the constraints Eq.(5c-5f)(9) in trajectory planning and use targeted approaches to eliminate them, respectively. Then, the original optimization problem is reformulated into an unconstrained program that can be further solved efficiently.

A. Feasibility Constraints

We adopt the discrete-time summation-type penalty term S_Σ to relax the feasibility constraints Eq. (9):

$$S_\Sigma(\mathbf{c}, \mathbf{T}) = \sum_{d \in \mathcal{D}} w_d \sum_{i=1}^n \sum_{j=1}^{M_i} \sum_{k=0}^{\lambda} P_{d,i,j,k}(\mathbf{c}_{i,j}, \mathbf{T}), \quad (62)$$

$$P_{d,i,j,k}(\mathbf{c}_{i,j}, \mathbf{T}) = \frac{\delta T_i}{\lambda} \bar{\omega}_k L_1(\mathcal{G}_{d,i,j,k}),$$

where w_d is the penalty weight corresponding to different kinds of constraints. $[\bar{\omega}_0, \bar{\omega}_1, \dots, \bar{\omega}_{\lambda-1}, \bar{\omega}_\lambda] =$

$[1/2, 1, \dots, 1, 1/2]$ are the quadrature coefficients from the trapezoidal rule [38] and $P_{d,i,j,k}$ is the violation penalty for a constraint point. Moreover, we define a first-order relaxation function $L_1(\cdot)$ to guarantee the continuous differentiability and non-negativity of penalty terms:

$$L_1(x) = \begin{cases} 0 & x \leq 0, \\ -\frac{1}{2a_0^3}x^4 + \frac{1}{a_0^2}x^3 & 0 < x \leq a_0 \\ x - \frac{a_0}{2} & a_0 < x. \end{cases} \quad (63)$$

Here $a_0 = 10^{-4}$ is the demarcation point. Such discrete penalty formulation ensures that continuous-time constraints Eq.(5g) are satisfied within an acceptable tolerance. Then, the trajectory optimization for vehicles is reformatted as follows:

$$\min_{\mathbf{c}, \mathbf{T}} \mathcal{J}(\mathbf{c}, \mathbf{T}) = J(\mathbf{c}, \mathbf{T}) + S_\Sigma(\mathbf{c}, \mathbf{T}) \quad (64a)$$

$$\text{s.t. } \boldsymbol{\sigma}_0^{[s-1]}(0) = \bar{\boldsymbol{\sigma}}_0, \boldsymbol{\sigma}_n^{[s-1]}(T_n) = \bar{\boldsymbol{\sigma}}_f, \quad (64b)$$

$$\boldsymbol{\sigma}_i^{[s-1]}(T_i) = \boldsymbol{\sigma}_{i+1}^{[s-1]}(0) = \bar{\boldsymbol{\sigma}}_i, 1 \leq i < n, \quad (64c)$$

$$\boldsymbol{\sigma}_{i,j}^{[\bar{d}]}(\delta T_i) = \boldsymbol{\sigma}_{i,j+1}^{[\bar{d}]}(0), 1 \leq i \leq n, 1 \leq j < M_i, \quad (64d)$$

$$T_i > 0, 1 \leq i \leq n. \quad (64e)$$

Without loss of generality, the gradients of the violation penalty at each constraint point on the trajectory are derived:

$$\begin{aligned} \frac{\partial P_{d,i,j,k}}{\partial \mathbf{c}_{i,j}} &= \frac{\partial P_{d,i,j,k}}{\partial \mathcal{G}_{d,i,j,k}} \frac{\partial \mathcal{G}_{d,i,j,k}}{\partial \mathbf{c}_{i,j}}, \\ \frac{\partial P_{d,i,j,k}}{\partial \mathbf{T}} &= \left(\mathbf{0}_{i-1}^\top, \frac{P_{d,i,j,k}}{T_i}, \mathbf{0}_{n-i}^\top \right)^\top + \frac{\partial P_{d,i,j,k}}{\partial \mathcal{G}_{d,i,j,k}} \frac{\partial \mathcal{G}_{d,i,j,k}}{\partial \mathbf{T}}, \\ \frac{\partial P_{d,i,j,k}}{\partial \mathcal{G}_{d,i,j,k}} &= \frac{\delta T_i}{\lambda} \bar{\omega}_k L_1'(\mathcal{G}_{d,i,j,k}). \end{aligned} \quad (65)$$

Since the gradients of the constraints $\mathcal{G}_{d,i,j,k}$ have been calculated in Sect. IV and Sect. V, we can also analytically obtain the gradients of the violation penalty $\partial P_{d,i,j,k}$ by the above propagation chain Eq.(65). Then, the gradients of the newly defined objective function $\mathcal{J}(\mathbf{c}, \mathbf{T})$ can be easily obtained in a similar way.

B. Equality Constraints

Before discussing the elimination of the equality constraints Eq.(64b)-(64d), we first decompose and reformulate Eq.(64c):

$$\boldsymbol{\sigma}_i(T_i) = \boldsymbol{\sigma}_{i+1}(0) = \mathbf{p}_i^g, \quad (66a)$$

$$\boldsymbol{\sigma}_i^{(1)}(T_i) = -\boldsymbol{\sigma}_{i+1}^{(1)}(0) = \mathbf{v}_i^g, \quad (66b)$$

$$\boldsymbol{\sigma}_i^{(\bar{d})}(T_i) = \boldsymbol{\sigma}_{i+1}^{(\bar{d})}(0) = \mathbf{0}_2, \quad (66c)$$

$$\|\mathbf{v}_i^g\|_2 = \bar{v}, \quad (66d)$$

$$\forall i \in \{1, 2, 3, \dots, n-1\}, \forall \bar{d} \in \{2, \dots, s-1\}. \quad (66e)$$

\mathbf{p}_i^g is the gear shifting position and \mathbf{v}_i^g is the final velocity before the shift. It is worth noting that the velocity direction is reversed before and after the shift and its magnitude is set to a small non-zero value \bar{v} to prevent singularities during optimization. For instance, \bar{v} is set to 0.05 in the actual implementation. Based on the optimality condition proved

in [39], the minimum control effort piece-wise polynomial coefficients \mathbf{c}_i are uniquely determined by the intermediate waypoints \mathbf{q}_i , the time interval of each piece, and the head and tail states:

$$\mathbf{M}_i(T_i) \mathbf{c}_i = \mathbf{b}_i, 1 \leq i \leq n, \quad (67)$$

where $\mathbf{M}_i(T_i) \in \mathbb{R}^{2M_i s \times 2M_i s}$ is an invertible banded matrix whose specific form can be found in [39]. $\mathbf{b}_{i \in \{1 \dots n\}} \in \mathbb{R}^{2M_i s \times 2}$ is defined as follows:

$$\begin{aligned} \mathbf{b}_1 &= (\bar{\boldsymbol{\sigma}}_0, \mathbf{q}_{1,1}, \mathbf{0}_{2 \times \bar{d}}, \dots, \mathbf{q}_{1, M_1-1}, \mathbf{0}_{2 \times \bar{d}}, \mathbf{p}_1^g, \mathbf{v}_1^g, \mathbf{0}_{2 \times (s-2)})^\top, \\ \mathbf{b}_n &= (\mathbf{p}_{n-1}^g, \mathbf{v}_{n-1}^g, \mathbf{0}_{2 \times (s-2)}, \mathbf{q}_{n,1}, \mathbf{0}_{2 \times \bar{d}}, \dots, \mathbf{q}_{n, M_n-1}, \mathbf{0}_{2 \times \bar{d}}, \bar{\boldsymbol{\sigma}}_f)^\top. \\ \mathbf{b}_i &= (\mathbf{p}_{i-1}^g, \mathbf{v}_{i-1}^g, \mathbf{0}_{2 \times (s-2)}, \mathbf{q}_{i,1}, \mathbf{0}_{2 \times \bar{d}}, \dots, \\ &\quad \mathbf{q}_{i, M_i-1}, \mathbf{0}_{2 \times \bar{d}}, \mathbf{p}_i^g, \mathbf{v}_i^g, \mathbf{0}_{2 \times (s-2)})^\top, 1 < i < n, \end{aligned} \quad (68)$$

where the degree of continuity \bar{d} is set to $2s-1$ to satisfy the optimality condition. Based on Eq.(67), we use the waypoints $\mathbf{q} = (\mathbf{q}_1, \dots, \mathbf{q}_n) \in \mathbb{R}^{2 \times \sum_{i=1}^n (M_i-1)}$, the time set \mathbf{T} , the gear shifting position $\mathbf{p}^g = (\mathbf{p}_1^g, \dots, \mathbf{p}_{n-1}^g) \in \mathbb{R}^{2 \times (n-1)}$ and the velocity $\mathbf{v}^g = (\mathbf{v}_1^g, \dots, \mathbf{v}_{n-1}^g) \in \mathbb{R}^{2 \times (n-1)}$ as decision variables in the optimization problem without sacrificing optimality, then the constraints Eq.(64b)(64d)(66a-66c) naturally satisfy:

$$\min_{\mathbf{q}, \mathbf{T}, \mathbf{p}^g, \mathbf{v}^g} \mathcal{J}(\mathbf{q}, \mathbf{T}, \mathbf{p}^g, \mathbf{v}^g) = \mathcal{J}(\mathbf{c}(\mathbf{q}, \mathbf{T}, \mathbf{p}^g, \mathbf{v}^g), \mathbf{T}) \quad (69a)$$

$$\text{s.t. } \|\mathbf{v}_i^g\|_2 = \bar{v}, 1 \leq i \leq n, \quad (69b)$$

$$T_i > 0, 1 \leq i \leq n. \quad (69c)$$

As stated in the work [39], the propagation of gradients from polynomial coefficients to time and waypoints can be computed with linear complexity, which is not presented repeatedly in this paper. Here, we derive the gradients w.r.t the gear shifting position and the velocity:

$$\frac{\partial \mathcal{J}}{\partial \mathbf{p}_i^g} = \left(\mathbf{M}_i^{-\top} \frac{\partial \mathcal{J}}{\partial \mathbf{c}_i} \right)^\top e_{(2M_i-1)s+1} + \left(\mathbf{M}_{i+1}^{-\top} \frac{\partial \mathcal{J}}{\partial \mathbf{c}_{i+1}} \right)^\top e_1, \quad (70)$$

$$\frac{\partial \mathcal{J}}{\partial \mathbf{v}_i^g} = \left(\mathbf{M}_i^{-\top} \frac{\partial \mathcal{J}}{\partial \mathbf{c}_i} \right)^\top e_{(2M_i-1)s+2} + \left(\mathbf{M}_{i+1}^{-\top} \frac{\partial \mathcal{J}}{\partial \mathbf{c}_{i+1}} \right)^\top e_2, \quad (71)$$

$$\forall i \in \{1, 2, 3, \dots, n-1\}.$$

e_k is a column vector of proper dimension, where the element of the k -th row is 1 and all others are 0. Furthermore, to satisfy the constraint Eq.(69b), we express $\mathbf{v}_i^g = (\bar{v} \cos \theta_i^g, \bar{v} \sin \theta_i^g)^\top$ in polar coordinates, where the physical meaning of θ_i^g is the direction of velocity before gear switching. Besides, we define the angle set $\boldsymbol{\theta}^g = (\theta_1^g, \theta_2^g, \dots, \theta_{n-1}^g)^\top \in \mathbb{R}^{n-1}$ for subsequent derivation and the cost function is transformed to $\mathcal{K}(\mathbf{q}, \mathbf{T}, \mathbf{p}^g, \boldsymbol{\theta}^g) = \mathcal{J}(\mathbf{q}, \mathbf{T}, \mathbf{p}^g, \mathbf{v}^g(\boldsymbol{\theta}^g))$. The gradient of the cost function \mathcal{K} w.r.t $\boldsymbol{\theta}^g$ can be obtained as follows:

$$\frac{\partial \mathcal{K}}{\partial \boldsymbol{\theta}_i^g} = (-\bar{v} \sin \theta_i^g, \bar{v} \cos \theta_i^g) \frac{\partial \mathcal{J}}{\partial \mathbf{v}_i^g}, 1 \leq i < n. \quad (72)$$

We eliminate all equation constraints in the original planning which is the basis for subsequent efficient optimization.

C. Positiveness Condition

To remove the strict positiveness condition Eq.(69c), we define an unconstrained virtual time $\boldsymbol{\tau} = [\tau_1, \dots, \tau_i, \dots, \tau_n]^\top \in$

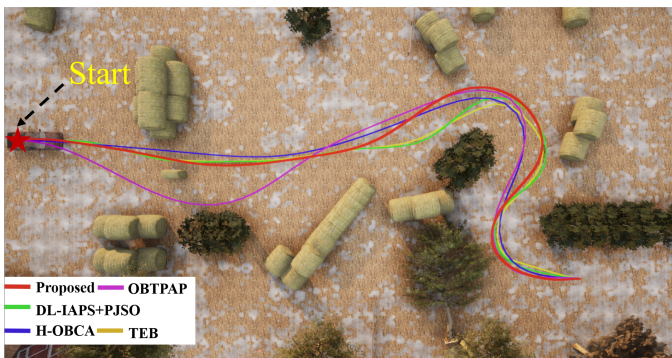


Fig. 5: The trajectory visualization.

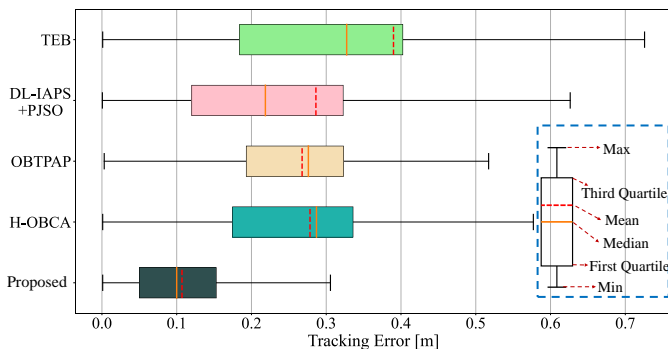


Fig. 6: Comparison of the tracking error profiles for the planned trajectories shown in Fig. 5.

\mathbb{R}^n and employ a diffeomorphism map [40] from $\tau_i \in \mathbb{R}$ to the real duration $T_i \in \mathbb{R}^+$:

$$T_i = \begin{cases} \frac{1}{2}\tau_i^2 + \tau_i + 1 & \tau_i > 0 \\ \frac{2}{\tau_i^2 - 2\tau_i + 2} & \tau_i \leq 0 \end{cases} \quad (73)$$

$\forall i \in \{1, 2, 3, \dots, n\}$.

Then, we use τ to replace the real time set \mathbf{T} so that the strict positiveness constraints Eq.(69c) are naturally satisfied. The corresponding reformulated optimization problem is as follows:

$$\min_{\mathbf{q}, \tau, \mathbf{p}^g, \theta^g} \mathcal{W}(\mathbf{q}, \tau, \mathbf{p}^g, \theta^g) = \mathcal{K}(\mathbf{q}, \mathbf{T}(\tau), \mathbf{p}^g, \theta^g). \quad (74)$$

The gradient can be propagated from T_i to τ_i :

$$\frac{\partial \mathcal{W}}{\partial \tau_i} = \begin{cases} (\tau_i + 1) \frac{\partial \mathcal{K}}{\partial T_i} & \tau_i > 0 \\ \frac{4(1 - \tau_i)}{(\tau_i^2 - 2\tau_i + 2)^2} \frac{\partial \mathcal{K}}{\partial T_i} & \tau_i \leq 0 \end{cases} \quad (75)$$

$\forall i \in \{1, 2, 3, \dots, n\}$.

The gradients w.r.t τ are efficiently calculated once we obtain the gradients w.r.t \mathbf{T} .

In summary, we have removed all constraints in the optimization and analytically derived the gradients. Finally, we robustly solve the transformed unconstrained optimization Eq.(74) via the quasi-Newton method [41].

VII. EVALUATIONS

The proposed method is evaluated both in simulation and in the real world. Benchmarks show that our planner outperforms state-of-the-art methods in terms of time efficiency and trajectory quality.

A. Simulations

All simulation experiments are conducted on a desktop computer running Ubuntu 18.04 with an Intel Core i7-10700 CPU and a GeForce RTX 2060 GPU. We perform simulation experiments based on the open-source physical simulator CARLA [42]. The proposed method is compared with four impressive methods specifically designed for motion planning of car-like robots in static unstructured environments, including OBTPAP [26], DL-IAPS+PJSO [15], H-OBCA [24] and Timed Elastic Bands (TEB) [43]. All methods use the bicycle model and are implemented in C++14 without parallel acceleration. OBTPAP [26] and H-OBCA [24] are solved by primal-dual interior-point method IPOPT [44]. DL-IAPS+PJSO [15] is implemented using OSQP [45]. The graph optimization solver G²o [46] is used for TEB [43]. Moreover, for fair comparisons, all planners use hybridA* [17] algorithm as their front-end to provide rough initial guesses for the subsequent optimization. The planned trajectory visualization is shown in Fig. 5. Additionally, the proposed planner, OBTPAP [26], DL-IAPS+PJSO [15] and TEB [43] use known global point clouds in the environment to construct safety constraints. H-OBCA [24] uses known convex polygons manually extracted from obstacles to construct its optimization formulation. All common parameters, including convergence conditions, dynamics constraints, and the ego vehicle dimensions, are set to the same for fairness. We use an MPC controller [47] that minimizes position and velocity errors to follow planned trajectories to measure the executable performance. We draw the tracking error of planned trajectories in Fig. 6, which visually demonstrates the superiority of the proposed method in terms of physical feasibility.

We conduct extensively quantitative assessments in many cases with different numbers of environmental obstacles and start-end distances (denote problem scale). Besides, the convergence tolerance of the optimization is set to 10^{-4} . Lots of comparison tests are performed in each case with random starting and ending states, and the average planning time under each test case is visualized in Fig. 8 to evaluate the real-time performance of planners. The histogram shows that our planner has an order-of-magnitude efficiency advantage over other algorithms, especially for large-scale trajectory generation. Furthermore, the results demonstrate the robustness against the problem scale and the number of environmental obstacles, thus allowing it to adapt to different scenarios. Moreover, we record physical dynamics statistics of planned trajectories including the mean of acceleration (abbreviated as M.A), jerk (M.JK) and tracking error (M.TE), as shown in Tab. I. The table show that our planner has the lowest control effort and the best human comfort in all cases. Additionally, the parametric form of the trajectory inherently guarantees the continuity of the state and its finite-dimensional derivatives,

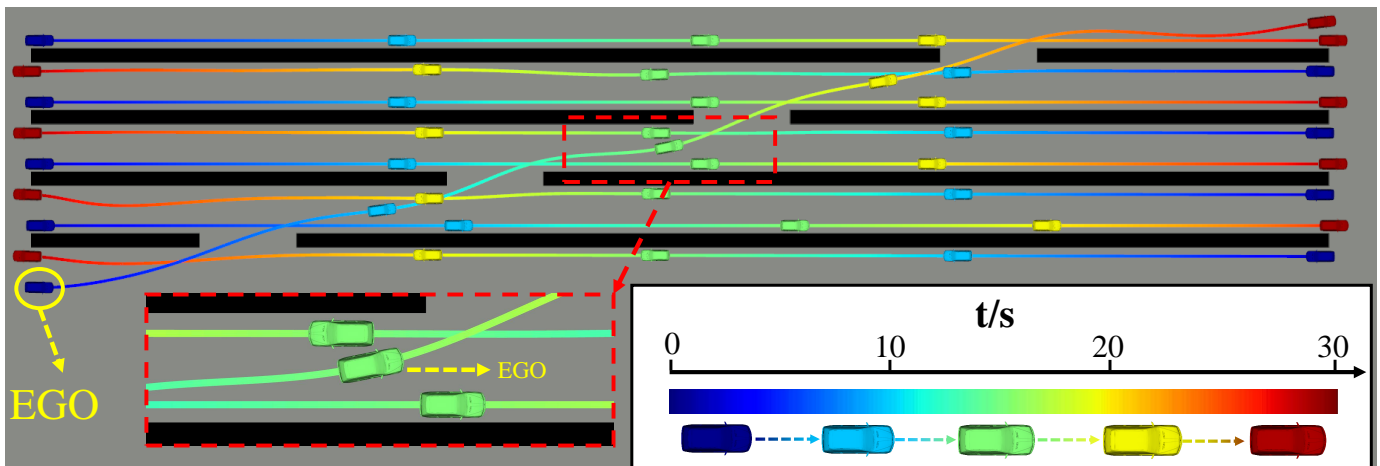


Fig. 7: Motion visualization in the dynamic environment, where the colors represent timestamps.

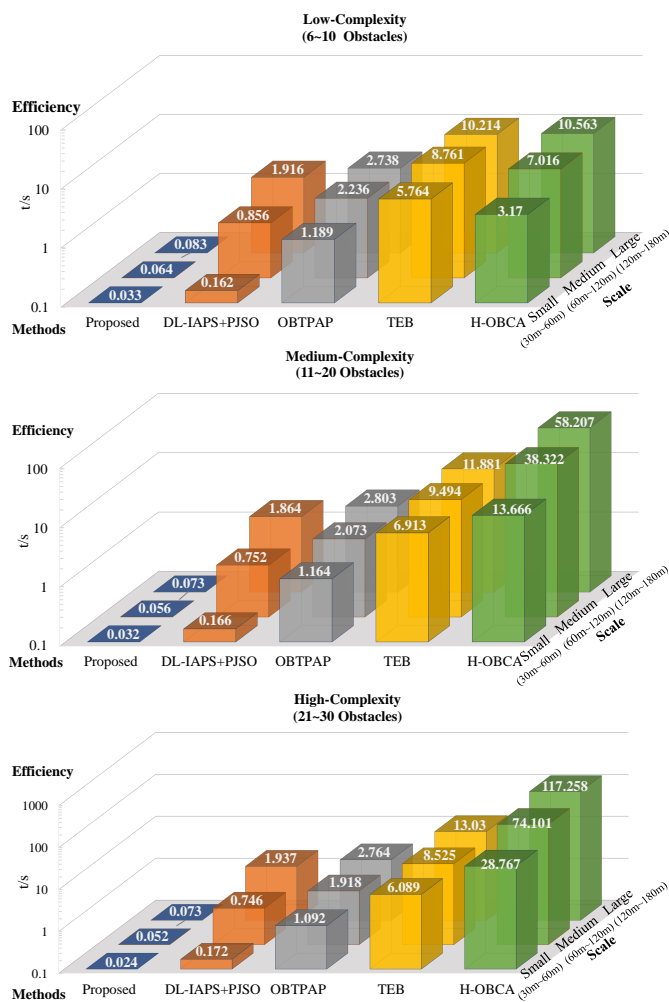


Fig. 8: Illustration of time efficiency comparisons.

which makes our trajectory easier to track than the above methods [15, 24, 26, 43] of discrete motion processes. It is worth mentioning that H-OBCA [24] also generates high-quality trajectories with dynamics statistics close to ours due to the accurate modeling of the problem. However, H-OBCA

[24] is inefficient and cannot be applied in real time, as shown in Fig. 8. The inherent problematic formulation of H-OBCA [24] causes it to be not robust to dense environments and imposes an intolerable computational burden as the number of obstacles increases.

We also validate the proposed planner in a $210m \times 50m$ dynamic unstructured environment where the ego vehicle is required to avoid static obstacles and the traffic flow consisting of eight other vehicles, as shown in Fig. 7. Since perception is not the focus of this paper, the environment and the trajectories of other vehicles are known to the planner. The maximum velocity of all vehicles is set to $10m/s$. The colors of vehicles and trajectories in Fig. 7 represent motion timestamps, which indicate the absence of spatial-temporal intersections between the ego vehicle and other moving objects, demonstrating dynamic safety. Thanks to full-dimensional modeling of objects, the ego vehicle has the ability to fully utilize the safe space to get through narrow areas, as the close-up shows. The trajectory length of the ego vehicle is $260m$, while the computation time is only $0.18s$, which demonstrates the efficiency of our planner in complex dynamic environments, especially for long-distance global trajectory generation.

B. Real-World Experiments

In addition to simulations, we also conduct real-world experiments to verify the feasibility of our planner on a real physical platform. The experimental site is a dense $40m \times 20m$ outdoor unstructured parking lot, as shown in Fig. 9. The moving robot is required to start from an initial state, go around obstacles, and eventually reverse into a parking space at a human-defined heading angle. The length of the whole track is about 42 meters. Real-world experiments are conducted on a SAIC-GM-Wuling Automobile Baojun E300² with dimensions of $2.9m \times 1.7m \times 1.6m$, a wheelbase of $2m$ and no GPS included, as shown in Fig. 10. A set of sensory elements including one stereo camera, four fisheye cameras, and twelve ultrasonic sensors are deployed on the platform for real-time localization, control, and data recording. Additionally, neither

²<https://www.sgmw.com.cn/E300.html/>

TABLE I: Comparison of Dynamic Statistics in Different Cases

Environments	Problem Scale	Small-Scale (30m ~ 60m)			Medium-Scale (60m ~ 120m)			Large-Scale (120m ~ 180m)		
	Method	M.A (m/s^2)	M.JK (m/s^3)	M.TE (m)	M.A (m/s^2)	M.JK (m/s^3)	M.TE (m)	M.A (m/s^2)	M.JK (m/s^3)	M.TE (m)
Low-Complexity (6 ~ 10 Obstacles)	Proposed	6.96	16.61	0.142	6.76	18.81	0.131	6.03	15.30	0.146
	OBTPAP	30.11	101.99	0.223	51.32	157.19	0.231	36.10	105.56	0.250
	DL-IAPS+PJSO	10.02	66.44	0.208	9.40	77.79	0.240	10.14	86.09	0.252
	H-OBCA	7.42	20.67	0.194	8.23	24.11	0.217	6.40	19.62	0.258
	TEB	16.27	380.52	0.348	15.74	427.35	0.338	14.96	363.07	0.321
Medium-Complexity (11 ~ 20 Obstacles)	Proposed	7.50	20.69	0.142	7.60	18.66	0.135	7.17	17.68	0.115
	OBTPAP	42.27	145.89	0.239	58.01	197.21	0.236	49.94	158.09	0.251
	DL-IAPS+PJSO	11.53	83.92	0.223	13.01	119.75	0.257	14.26	140.55	0.254
	H-OBCA	7.85	21.69	0.216	8.88	26.25	0.213	7.05	20.57	0.231
	TEB	18.72	466.93	0.348	21.94	614.42	0.343	21.32	707.91	0.357
High-Complexity (21 ~ 30 Obstacles)	Proposed	7.53	17.95	0.127	7.97	19.49	0.120	6.97	17.56	0.126
	OBTPAP	36.54	128.29	0.230	43.90	157.32	0.247	57.03	193.75	0.251
	DL-IAPS+PJSO	12.25	94.43	0.210	16.24	155.38	0.259	13.92	134.74	0.268
	H-OBCA	8.09	23.58	0.195	8.17	25.77	0.230	7.05	21.49	0.248
	TEB	19.67	493.70	0.352	23.42	607.32	0.416	19.89	584.01	0.365

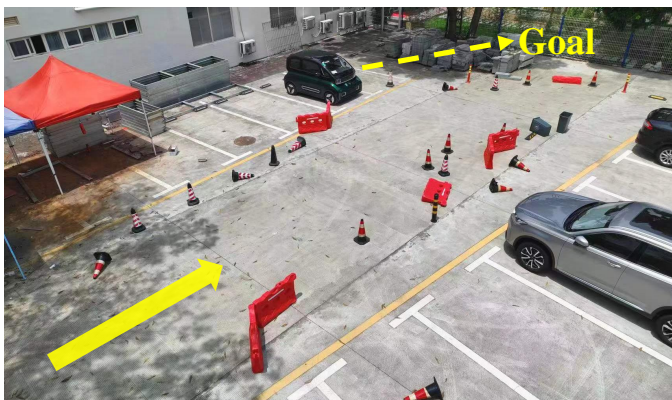


Fig. 9: The real-world experiment site.



Fig. 10: The experimental platform.

high precision LIDAR nor precise external positioning systems are used in our real-world experiments. All modules are implemented in C++ and deployed on TI TDA4 Chip (64-bit Dual Arm Cortex-A72 @2000MHz)³ configured with QNX

³<https://www.ti.com/product/TDA4VM>

TABLE II: Dynamic Statistics in Real-World Experiments

Statistics	Mean	Max	STD.
Forward.Vel. (m/s)	1.53	1.95	0.52
Backward.Vel. (m/s)	0.45	0.50	0.10
Forward.Jerk. (m/s^3)	0.25	6.95	0.50
Backward.Jerk (m/s^3)	0.18	7.07	0.55

Operating System. During the trajectory planning, the vehicle shape was expanded by $0.25m$ to ensure safety during actual execution in the presence of unavoidable control and positioning errors. The maximum forward and backward speeds are set to $2m/s$ and $0.5m/s$, respectively. The time weight w_T is set to 50 to ensure the aggressiveness of the trajectory. The motion of the ego vehicle is visualized in Fig. 11, which demonstrates that the ego vehicle can follow the planned trajectory to avoid obstacles and eventually reverse into a parking space with the user-given heading angle. Furthermore, dynamic evaluation metrics are quantified in Tab. II. As we can see, the ego vehicle maintains a relatively high speed throughout to reach the target state without exceeding the dynamic limits while keeping a low jerk to ensure the comfort of passengers. Finally, more demonstrations can be found in the supplementary material.

VIII. CONCLUSION

This paper proposes an efficient spatial-temporal trajectory planning for car-like robots. We use polynomials in flat space to parameterize trajectories such that fewer decision variables characterize a continuous trajectory with higher-order information. Moreover, the spatial-temporal joint optimization of the trajectory also guarantees better optimality. We decompose ambient point clouds and free space to construct a safe driving corridor, thus modeling geometric constraints used to ensure static obstacle avoidance. To cope with dynamic environments,

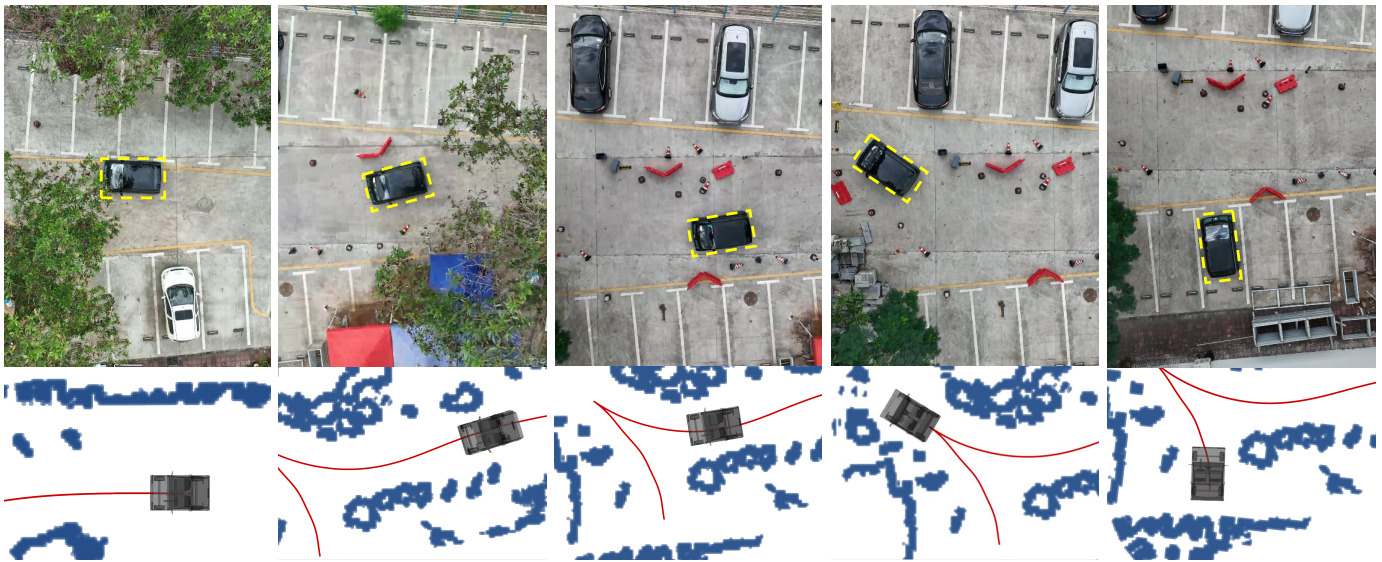


Fig. 11: The motion diagram of the ego vehicle in the real-world experiment, where the red curve is the execution trajectory.

we constrain the signed distances between the ego vehicle and moving objects to achieve full-dimensional obstacle avoidance. Benchmark results with state-of-the-art methods demonstrate the superiority of our method in terms of time efficiency and trajectory quality. Real-world experiments are also conducted to validate the effectiveness of the proposed method on a real platform.

In the future, we will explore the application of the method to multiple robots and extend the principle to other motion models. In addition, we will focus on motion planning for rugged terrain in the field, such as going up and down hills.

REFERENCES

- [1] C. Urmson, J. Anhalt, D. Bagnell, C. Baker, R. Bittner, M. Clark, J. Dolan, D. Duggins, T. Galatali, C. Geyer *et al.*, “Autonomous driving in urban environments: Boss and the urban challenge,” *Journal of field Robotics*, vol. 25, no. 8, pp. 425–466, 2008.
- [2] J. Ziegler and C. Stiller, “Spatiotemporal state lattices for fast trajectory planning in dynamic on-road driving scenarios,” in *2009 IEEE/RSJ International Conference on Intelligent Robots and Systems*. IEEE, 2009, pp. 1879–1884.
- [3] M. Rufli and R. Siegwart, “On the design of deformable input/state-lattice graphs,” in *2010 IEEE International Conference on Robotics and Automation*. IEEE, 2010, pp. 3071–3077.
- [4] M. McNaughton, C. Urmson, J. M. Dolan, and J.-W. Lee, “Motion planning for autonomous driving with a conformal spatiotemporal lattice,” in *2011 IEEE International Conference on Robotics and Automation*. IEEE, 2011, pp. 4889–4895.
- [5] S. M. LaValle *et al.*, “Rapidly-exploring random trees: A new tool for path planning,” 1998.
- [6] A. Shkolnik, M. Walter, and R. Tedrake, “Reachability-guided sampling for planning under differential constraints,” in *2009 IEEE International Conference on Robotics and Automation*. IEEE, 2009, pp. 2859–2865.
- [7] S. Karaman and E. Frazzoli, “Sampling-based algorithms for optimal motion planning,” *The international journal of robotics research*, vol. 30, no. 7, pp. 846–894, 2011.
- [8] D. J. Webb and J. van den Berg, “Kinodynamic RRT*: Asymptotically optimal motion planning for robots with linear dynamics,” in *2013 IEEE International Conference on Robotics and Automation*, May 2013, pp. 5054–5061.
- [9] L. Han, Q. H. Do, and S. Mita, “Unified path planner for parking an autonomous vehicle based on RRT,” in *2011 IEEE International Conference on Robotics and Automation*. IEEE, 2011, pp. 5622–5627.
- [10] L. Palmieri, S. Koenig, and K. O. Arras, “RRT-based nonholonomic motion planning using any-angle path biasing,” in *2016 IEEE International Conference on Robotics and Automation (ICRA)*. IEEE, 2016, pp. 2775–2781.
- [11] N. Seegmiller, J. Gassaway, E. Johnson, and J. Towler, “The maverick planner: An efficient hierarchical planner for autonomous vehicles in unstructured environments,” in *2017 IEEE/RSJ International Conference on Intelligent Robots and Systems (IROS)*. IEEE, 2017, pp. 2018–2023.
- [12] M. Elbanhawi and M. Simic, “Sampling-based robot motion planning: A review,” *Ieee access*, vol. 2, pp. 56–77, 2014.
- [13] Z. Zhu, E. Schmerling, and M. Pavone, “A convex optimization approach to smooth trajectories for motion planning with car-like robots,” in *2015 54th IEEE conference on decision and control (CDC)*. IEEE, 2015, pp. 835–842.
- [14] C. Liu, C.-Y. Lin, and M. Tomizuka, “The convex feasible set algorithm for real time optimization in motion planning,” *SIAM Journal on Control and optimization*, vol. 56, no. 4, pp. 2712–2733, 2018.
- [15] J. Zhou, R. He, Y. Wang, S. Jiang, Z. Zhu, J. Hu, J. Miao, and Q. Luo, “Autonomous driving trajectory optimization with dual-loop iterative anchoring path smoothing and piecewise-jerk speed optimization,” *IEEE Robotics and Automation Letters*, vol. 6, no. 2, pp. 439–446, 2021.
- [16] A. Domahidi and J. Jerez, “Forces professional. embotech gmbh (<http://embotech.com/forces-pro>),” *t uly (cit. on p. 30)*, 2014.
- [17] D. Dolgov, S. Thrun, M. Montemerlo, and J. Diebel, “Path planning for autonomous vehicles in unknown semi-structured environments,” *The International Journal of Robotics Research*, vol. 29, no. 5, pp. 485–501, 2010.
- [18] K. Kondak and G. Hommel, “Computation of time optimal movements for autonomous parking of non-holonomic mobile platforms,” in *Proceedings 2001 ICRA. IEEE International Conference on Robotics and Automation (Cat. No. 01CH37164)*, vol. 3. IEEE, 2001, pp. 2698–2703.
- [19] H. Shin, D. Kim, and S.-E. Yoon, “Kinodynamic comfort trajectory planning for car-like robots,” in *2018 IEEE/RSJ International Conference on Intelligent Robots and Systems (IROS)*. IEEE, 2018, pp. 6532–6539.
- [20] B. Li and Z. Shao, “Simultaneous dynamic optimization: A trajectory planning method for nonholonomic car-like robots,” *Advances in Engineering Software*, vol. 87, pp. 30–42, 2015.
- [21] B. Li and Z. Shao, “A unified motion planning method for parking an autonomous vehicle in the presence of irregularly placed obstacles,” *Knowledge-Based Systems*, vol. 86, pp. 11–20, 2015.
- [22] K. Bergman and D. Axehill, “Combining homotopy methods and numerical optimal control to solve motion planning problems,” in *2018 IEEE Intelligent Vehicles Symposium (IV)*. IEEE, 2018, pp. 347–354.
- [23] S. Shi, Y. Xiong, J. Chen, and C. Xiong, “A bilevel optimal motion planning (bomp) model with application to autonomous parking,” *International Journal of Intelligent Robotics and Applications*, vol. 3, no. 4, pp. 370–382, 2019.
- [24] X. Zhang, A. Liniger, A. Sakai, and F. Borrelli, “Autonomous parking

- using optimization-based collision avoidance,” in *2018 IEEE Conference on Decision and Control (CDC)*. IEEE, 2018, pp. 4327–4332.
- [25] R. He, J. Zhou, S. Jiang, Y. Wang, J. Tao, S. Song, J. Hu, J. Miao, and Q. Luo, “TDR-OBICA: A reliable planner for autonomous driving in free-space environment,” in *2021 American Control Conference (ACC)*. IEEE, 2021, pp. 2927–2934.
- [26] B. Li, T. Acarman, Y. Zhang, Y. Ouyang, C. Yaman, Q. Kong, X. Zhong, and X. Peng, “Optimization-based trajectory planning for autonomous parking with irregularly placed obstacles: A lightweight iterative framework,” *IEEE Transactions on Intelligent Transportation Systems*, 2021.
- [27] P. E. Gill, W. Murray, and M. A. Saunders, “Snopt: An sqp algorithm for large-scale constrained optimization,” *SIAM review*, vol. 47, no. 1, pp. 99–131, 2005.
- [28] X. Zhang, A. Liniger, and F. Borrelli, “Optimization-based collision avoidance,” *IEEE Transactions on Control Systems Technology*, vol. 29, no. 3, pp. 972–983, 2021.
- [29] M. da Silva Arantes, C. F. M. Toledo, B. C. Williams, and M. Ono, “Collision-free encoding for chance-constrained nonconvex path planning,” *IEEE Transactions on Robotics*, vol. 35, no. 2, pp. 433–448, 2019.
- [30] J. Reeds and L. Shepp, “Optimal paths for a car that goes both forwards and backwards,” *Pacific journal of mathematics*, vol. 145, no. 2, pp. 367–393, 1990.
- [31] R. M. Murray, M. Rathinam, and W. Sluis, “Differential flatness of mechanical control systems: A catalog of prototype systems,” in *Proceedings of the 1995 ASME International Congress and Exposition*, 1995.
- [32] I. Bae, J. Moon, J. Jhung, H. Suk, T. Kim, H. Park, J. Cha, J. Kim, D. Kim, and S. Kim, “Self-driving like a human driver instead of a robocar: Personalized comfortable driving experience for autonomous vehicles,” *arXiv preprint arXiv:2001.03908*, 2020.
- [33] X. Zhong, Y. Wu, D. Wang, Q. Wang, C. Xu, and F. Gao, “Generating large convex polytopes directly on point clouds,” *ArXiv*, vol. abs/2010.08744, 2020.
- [34] D. Avis, K. Fukuda, and S. Picozzi, “On canonical representations of convex polyhedra,” in *Mathematical Software*. World Scientific, 2002, pp. 350–360.
- [35] E. Gilbert, D. Johnson, and S. Keerthi, “A fast procedure for computing the distance between complex objects in three-dimensional space,” *IEEE Journal on Robotics and Automation*, vol. 4, no. 2, pp. 193–203, 1988.
- [36] S. Cameron and R. Culley, “Determining the minimum translational distance between two convex polyhedra,” in *Proceedings. 1986 IEEE International Conference on Robotics and Automation*, vol. 3, 1986, pp. 591–596.
- [37] M. Lutz and T. Meurer, “Efficient formulation of collision avoidance constraints in optimization based trajectory planning and control,” in *2021 IEEE Conference on Control Technology and Applications (CCTA)*. IEEE, 2021, pp. 228–233.
- [38] W. Tribbey, “Numerical recipes,” *Software engineering notes.*, vol. 35, no. 6, 2010-11-27.
- [39] Z. Wang, X. Zhou, C. Xu, and F. Gao, “Geometrically constrained trajectory optimization for multicopters,” *IEEE Transactions on Robotics*, pp. 1–10, 2022.
- [40] J. Leslie, “On a differential structure for the group of diffeomorphisms,” *Topology*, vol. 6, no. 2, pp. 263–271, 1967.
- [41] D. C. Liu and J. Nocedal, “On the limited memory bfgs method for large scale optimization,” *Mathematical programming*, vol. 45, no. 1-3, pp. 503–528, 1989.
- [42] A. Dosovitskiy, G. Ros, F. Codevilla, A. Lopez, and V. Koltun, “Carla: An open urban driving simulator,” in *Conference on robot learning*. PMLR, 2017, pp. 1–16.
- [43] C. Rösmann, F. Hoffmann, and T. Bertram, “Kinodynamic trajectory optimization and control for car-like robots,” in *2017 IEEE/RSJ International Conference on Intelligent Robots and Systems (IROS)*. IEEE, 2017, pp. 5681–5686.
- [44] A. Wächter and L. T. Biegler, “On the implementation of an interior-point filter line-search algorithm for large-scale nonlinear programming,” *Mathematical programming*, vol. 106, no. 1, pp. 25–57, 2006.
- [45] B. Stellato, G. Banjac, P. Goulart, A. Bemporad, and S. Boyd, “Osqp: An operator splitting solver for quadratic programs,” *Mathematical Programming Computation*, vol. 12, no. 4, pp. 637–672, 2020.
- [46] R. Kümmerle, G. Grisetti, H. Strasdat, K. Konolige, and W. Burgard, “G2o: A general framework for graph optimization,” in *2011 IEEE International Conference on Robotics and Automation*, 2011, pp. 3607–3613.
- [47] J. Kong, M. Pfeiffer, G. Schildbach, and F. Borrelli, “Kinematic and dynamic vehicle models for autonomous driving control design,” in *2015 IEEE intelligent vehicles symposium (IV)*. IEEE, 2015, pp. 1094–1099.